

Modelling extreme water levels using intertidal topography and bathymetry derived from multispectral satellite images

Wagner L.L. Costa¹, Karin R. Bryan¹, Giovanni Coco²

¹School of Science, University of Waikato, 124 Hillcrest Road, E-F link, Hamilton, New Zealand.

5 ²School of Environment, University of Auckland, Auckland, New Zealand.

Correspondence to: Wagner L.L. Costa (wc119@students.waikato.ac.nz)

Abstract. Topographic and bathymetric data are essential for accurate predictions of flooding in estuaries because water depth and elevation data are fundamental components of the shallow-water hydrodynamic equations used in e.g. models for storm surge and tides. Where LiDAR or in-situ acoustic surveys are unavailable, recent efforts have centred on using satellite images to derive bathymetry (SDB) and topography (SDT). This work is aimed at (1) determining the accuracy of SDT and (2) assessing the suitability of the SDT and SDB for surge/tidal modelling of estuaries. The SDT was created by extracting the waterline as it tracks over the topography with changing tides. The method was applied to 4 different estuaries in New Zealand: Whitianga, Maketū, Ōhiwa and Tauranga. Results show that the waterline method provides similar topography to the LiDAR with a root-mean-squared error equal to 0.2 m, and it is slightly improved when two correction methods are applied to the topography derivations: the removal of statistical bias (2 cm improvement) and hydrodynamic modelling correction of waterline elevation (1 cm improvement). Finally, the use of SDT in numerical simulations of surge levels was assessed for Tauranga Harbour in four different scenarios that explore different ways of incorporating the SDT compared to modelling using topographic data collected using non-satellite survey methods. One of these scenarios trials replacing the subtidal bathymetry with SDB, derived using the well-known ratio-log method (so that only satellite information is used in surge modelling). For Tauranga Harbour, using SDT and SDB in hydrodynamic models does not result in significant differences in predicting high water levels when compared with the scenario modelled using surveyed bathymetry.

1 Introduction

Coastal flooding has become increasingly concerning because of growing storm intensity (Emanuel, 2005; Webster et al., 2005; Sobel et al., 2016) and sea level rise, which will potentially increase the risk exposure of coastal communities (Nicholls and Cazenave, 2010; Oppenheimer et al., 2019). In practice, predicting flooding depends on understanding the contribution from the astronomical tide, storm surge, wave run-up, changes in the sea level and, in some cases, the fluvial discharge and vertical land motion. In coastal zones, these processes can interfere with each other, for example, in tide-surge interactions (Spicer et al., 2019; Wankang et al., 2019; Du et al., 2018). In the case of estuaries, bathymetric and topographic data are essential for coastal risk assessment (Parodi et al., 2020) because they influence the accuracy of water level predictions (Cea and French,

30 2012; Pedrozo-Acuña et al., 2012; Falcão et al., 2013; Mohammadian et al., 2022). Water depth is a fundamental component in the shallow-water hydrodynamic equations used in extreme water level modelling. Together with the estuary's geometry and length — which can cause shoaling and choking — and bed-shear stress — which reduces energy due to its effect on friction, bathymetry and topography control the amplitude and phase (timing) of the propagating tide. The estuary's morphology is also fundamental for studying the tidal response to sea level rise (Khojasteh et al., 2020, 2021; Du et al., 2018).

35

The methods used to measure bathymetry and topography in coastal zones have evolved rapidly. In estuaries, there are permanently inundated areas (which are generally shallow) and intertidal zones, which are areas flooded and exposed by the tide. Here we define the terms bathymetry and topography to reflect permanently-inundated and intertidal areas respectively. Currently, there are four types of systems for measuring these: ship-based systems (e.g., single-beam and multibeam
40 echosounders), non-imaging active remote sensing (e.g. LiDAR), imaging active remote sensing (e.g. synthetic aperture radar — SAR), and imaging passive remote sensing (e.g. optical systems) (Jawak et al., 2015; Salameh et al., 2019; Ashphaq et al., 2021). Traditionally, the most commonly-used systems are echosounders and LiDAR. Both produce highly accurate data; however, several factors constrain their application, such as economic cost, staffing costs, inaccessibility of remote areas, and environmental conditions (e.g., low tide navigational restrictions). Consequently, approximately 70% of the world's coastal
45 areas have not been surveyed or surveyed recently (IHO, 2020).

Space-borne remote sensing techniques overcome the limitations of traditional techniques and can provide topographic and bathymetric data for a wide range of environments, including areas that are more difficult to measure such as remote shallow coastal waters (Lyzenga, 1985; Ehses and Rooney, 2015; Caballero and Stumpf, 2019) and extensive intertidal areas (Bishop-
50 Taylor et al., 2019; Fitton et al., 2021). Several methods are used to derive bathymetric data — hereafter called satellite-derived bathymetry (SDB) — in shallow waters (i.e., between 0–15m depth) using imaging passive remote sensing of reflectance (Ashphaq et al., 2021). Most of methods are developed around the process of light attenuation through the water column, and fall into two approaches. Empirical methods use direct observations of water depth in the study area to calibrate the reflectance-to-depth relationship (Stumpf et al., 2003; Caballero and Stumpf, 2019), and physics-based inversion algorithms use physical
55 processes/models to solve for water depth (e.g., radiative transfer models) without the need for in situ calibration data (Lee et al., 1998, 1999; Kerr and Purkis, 2018).

In the present manuscript, we focused on empirical methods to obtain the SDB, and use the ratio-log method proposed by Stumpf et al. (2003). Its main limitations are the requirement of in situ bathymetric data for calibration and the sensitivity of
60 the Stumpf method to environmental conditions that can change bottom and water reflectance — e.g., water turbidity and variation in the benthic substrates — that often occur in enclosed seas, bays and estuaries (Morris et al., 2021). Some studies have proposed techniques to tackle empirical issues (e.g., Caballero and Stumpf, 2020; Geyman and Maloof, 2019). Caballero and Stumpf (2020) have adjusted reflectance ratios to reduce the effects of water turbidity and calculated the maximum

chlorophyll index first to identify pixels containing floating and submerged vegetation and then remove these pixels from
65 further implementation of the ratio-log formula. Geyman and Maloof (2019) have implemented the cluster-based regression
algorithm to deal with different bottom substrates, first segmenting the satellite image into zones of spectral homogeneity and
then calibrating the log-linear colour-to-depth relationship separately for each class.

In intertidal regions, remote sensing can also be used to obtain satellite-derived topography (SDT) — and the waterline method
70 is the most commonly applied. The method was first applied to SAR images (Mason and Davenport, 1996), and recently also
to multispectral space-borne images (Khan et al., 2019; Salameh et al., 2020; Fitton et al., 2021). The technique functions by
detecting the edge between the flooded and exposed intertidal zone in multiple images (i.e., the waterline) and assigning a
height to each waterline by using the local tidal level at the time of image acquisition. The tidal level can be acquired by a
numerical tide model (e.g., Khan et al., 2019; Kang et al., 2020; Salameh et al., 2020) or from a local tide gauge (Mason and
75 Davenport, 1996; Salameh et al., 2020). The resulting collection of waterlines is interpolated over the intertidal domain,
generating a digital elevation model (DEM). The approach assumes that estuary morphology does not change between images
and has a gentle slope. The main disadvantages of this method are the dependence of accuracy on the number of images used
in processing and the reduced performance in sites with complex morphology, i.e., variable terrain slopes within the intertidal
80 zone (Liu et al., 2013; Salameh et al., 2019, 2020). Other methods used to derive topography in intertidal zones are the
interferometric SAR (Li and Goldstein, 1990), satellite radar altimetry (Salameh et al., 2018) and near-infrared logistic
approach (Bué et al., 2020).

As remote-sensing techniques have developed, cloud computation and storage systems such as Google Earth Engine (Gorelick
et al., 2017) have also advanced considerably. Consequently, scientists now have an enhanced capacity to quickly manage
85 large geographical datasets, allowing global-scale studies in coastal science to evolve rapidly (e.g., Murray et al., 2019; Vos
et al., 2019; Bishop-Taylor et al., 2019). For instance, databases now exist on the distribution of and changes to global tidal
flats (Murray et al., 2019), as well as a global estimate of coastline position (Almeida et al., 2021; Vos et al., 2019). Satellite-
derived bathymetry (SDB) and topography (SDT) techniques are now routinely applied over extensive areas (e.g., Traganos
et al., 2018; Bishop-Taylor et al., 2019; Fitton et al., 2021). Despite the vast and growing application of SDB and SDT methods
90 to coastal science and engineering (Turner et al., 2021), it is not yet clear whether the accuracy of the resulting estimates is
suitable for modelling extreme water levels in coastal areas (e.g., estuaries and bays). Only limited studies exist relating to
SDB and SDT and numerical modelling — generally aimed at using the model to assign the waterline height (Khan et al.,
2019; Salameh et al., 2020; Fitton et al., 2021). For instance, Mason et al. (2010) used SDT to calibrate a morphodynamical
model.

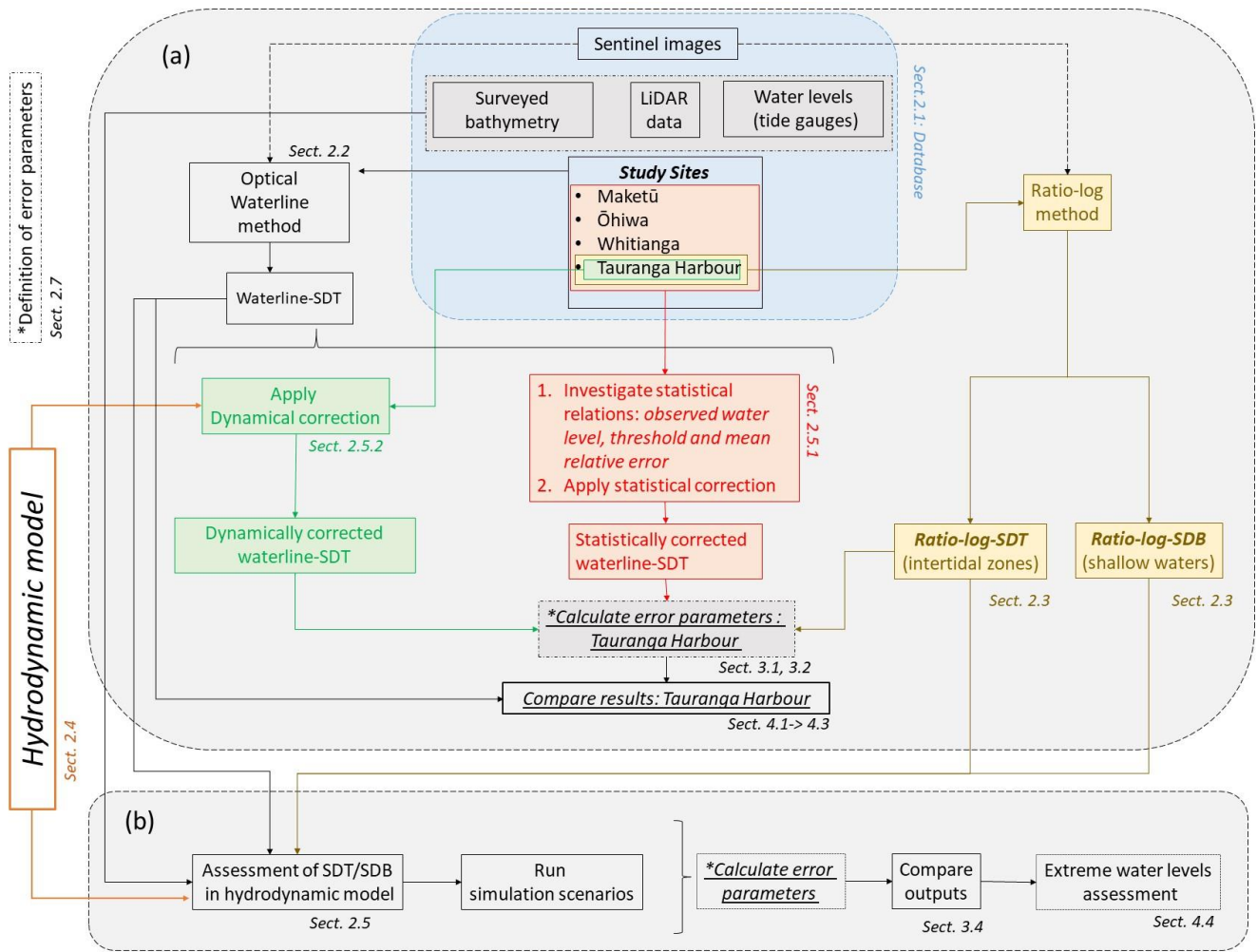
95

Our study aims to evaluate whether SDT and SDB can replace surveyed data as a boundary condition in hydrodynamic modelling — focusing on predicting high water levels (surges and extreme high tides) in estuaries with complex morphology.

We have three specific objectives:

1. To determine whether satellite imagery can be used to extract accurate SDT;
- 100 2. To investigate the main source of errors in the satellite-derived techniques; and,
3. To assess the use of SDT and SDB for hydrodynamic modelling of estuaries compared to data derived from traditional methods.

This manuscript is divided into two main parts, as illustrated in Figure 1: (a) the SDT and SDB framework and (b) the hydrodynamic modelling assessment. Firstly, we present the methods (Sect. 2), where we show the study sites and database
105 (Sect. 2.1), the applied SDT and SDB methods (Sect. 2.2 and 2.3), and the specifications of the hydrodynamic modelling used in Sect. 2.5.2 and Sect. 2.6. Then we show the approaches we used to improve the SDT obtained using our framework (Sect. 2.5), how we assess the water level simulations using SDT and SDB (Sect 2.6), and how we assess our framework performance (Sect. 2.7). In Sect. 3, we show our results, the waterline-derived and the ratio-log-derived intertidal elevation (Sect. 3.1); the
110 statistical and dynamical corrections (Sect. 3.2); the prediction of high water levels using SDT and SDB (Sect. 3.3). In Sect. 4, we discuss our main findings: the advantages and limitations of our proposed SDT and SDB framework and correction approaches (Sect.4.1 and 4.2); the comparison between SDTs derived from the waterline and ratio-log methods (Sect.4.3); the hydrodynamic modelling assessment (Sect.4.4); and, in Sect. 5, the conclusion.



115 **Figure 1: A flow chart showing the steps taken to derive the SDT/SDB (a) and to test its utility in modelling (b).**

2 Methods

2.1 Study site and database

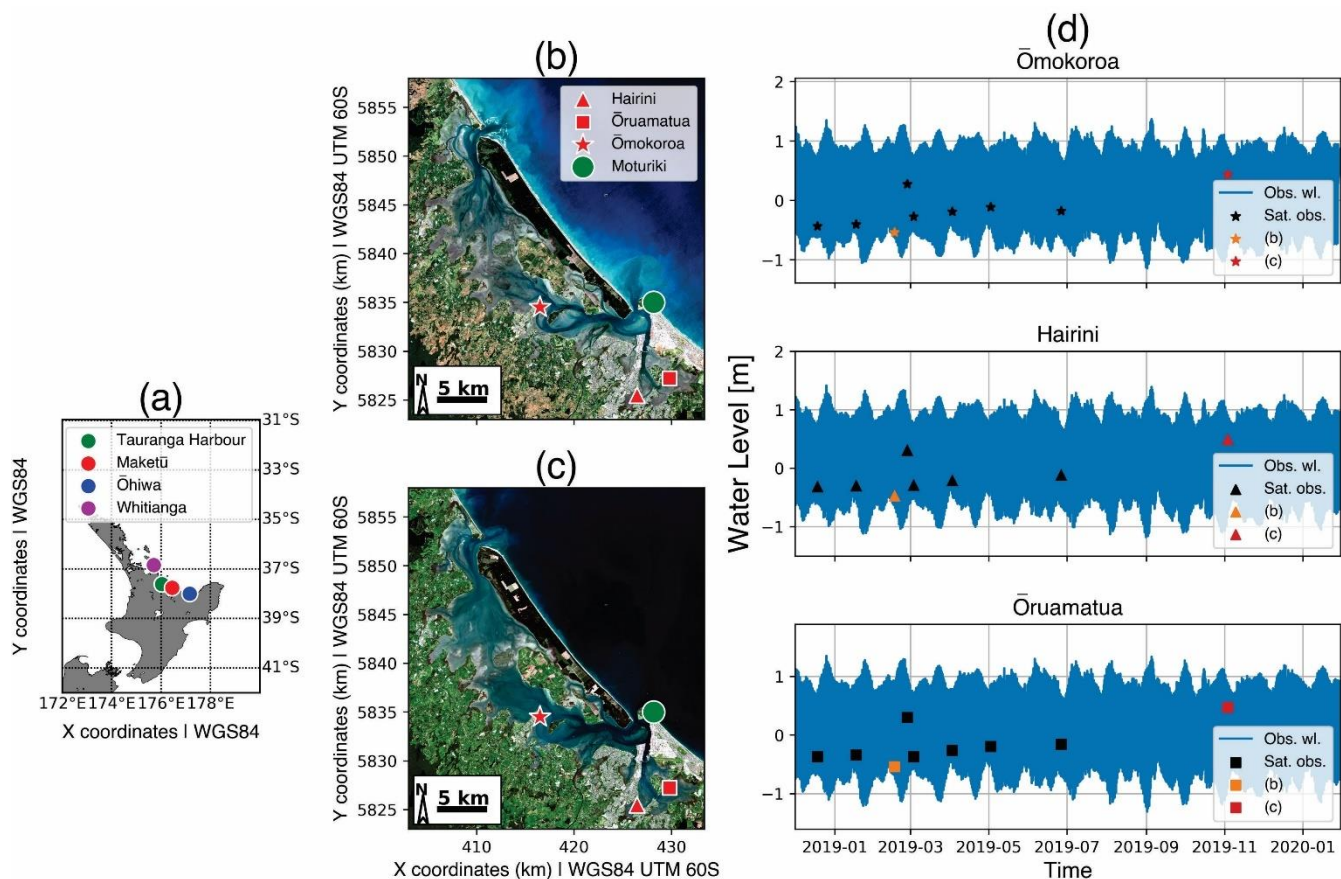
120 The study areas are four estuaries on the east coast of Aotearoa New Zealand's North Island. Three are in the Bay of Plenty region: Tauranga, Ōhiwa and Maketū harbours and one in the Coromandel: Whitianga harbour, Figure 2A. The studied sites have micro-tidal regimes — the spring tidal range varies between 1.4 m to 1.9 m within estuaries – and the equinoctial spring tides combined with severe storm surges drive the extreme sea levels (Rueda et al., 2019; Stephens et al., 2020). In New Zealand, the surges caused by storms usually add < 0.5 m to the water level, but the maximum surge ever registered was 2.29 m (Stephens et al., 2020). In Tauranga Harbour, the maximum storm-driven surge ever recorded is equal to 0.88 m (Stephens et al., 2020), and the tide can be attenuated by 10% to 17% (M2 component) when the tidal wave propagates through the

125 estuary (Tay et al., 2013). The water level inside the study site estuaries is not considered to be substantially affected by the
action of waves (i.e., wave set-up) because all of them are enclosed coastal lagoons with restricted entrances. All four estuaries
have large intertidal areas covering from 58% to 84% of the estuaries' total area (Hume et al., 2016); see Table 1. The extent
of the tidal flats is evident in Tauranga Harbour by comparing low (e.g., Figure 2b) and high (e.g., Figure 2c) tide satellite
130 Harbours (the latter was studied in Ha et al. (2020)). Detailed images of the intertidal zones in Tauranga Harbour and its
seagrass banks and mangroves can be seen in Figure S3.

Imagery, tidal levels and topography data (e.g., LiDAR) were acquired to implement and validate the SDT techniques. For the
Bay of Plenty region, historical tide levels were downloaded from the Bay of Plenty Council data portal
135 (<https://envdata.boprc.govt.nz/>); the topography data consisted of the LiDAR survey for which a 1×1m resolution dataset was
available on the Land Information New Zealand data portal (<https://data.linz.govt.nz/>). For Whitianga, we acquired water level
time series and elevation data (LiDAR) through the Thames-Coromandel District Council's website (<http://www.tcdc.govt.nz/>).
The LiDAR data have an accuracy of ± 0.2 m in the vertical and ± 0.6 m in the horizontal with 95% confidence for the Bay of
Plenty. All LiDAR data were converted to the local vertical datum (i.e., Moturiki 1953), which is 0.13 m below mean sea level
140 (MSL), using the GEOID elevation grids available in the LINZ data portal.

We used European Space Agency (ESA) Copernicus Sentinel satellite images accessed through Google Earth Engine (Gorelick
et al., 2017) from spacecraft Sentinel 2A and B, product type level-2A. The Sentinel-2 products are composed of elementary
tiles, which are 100×100 km² ortho-images in the UTM/WGS84 projection, with a revisit frequency of 5 days in the Aotearoa
145 New Zealand region. The level-2A product type provides bottom-of-atmosphere (BOA) images, which are already corrected
for the effects of the top-atmosphere, terrain and cirrus cloud using the Sen2Cor processing tool (ESA). Each image has the
spectral resolution of 12 bands with spatial resolution differing between 10, 20 and 60 m depending on the band. Here we used
the green (band 3, 560 nm), blue (band 2, 490 nm) and near-infrared (band 8, 842 nm) bands, all of them with 10 m spatial
resolution.

150 In summary, a complete set of LiDAR, tidal gauge observations and a satellite image was obtained for each estuary. For
example, the Tauranga Harbour dataset is shown in Figure 2: the location of the tide gauges (Ōmokoroa, Hairini and Ōruamatua)
and the intertidal exposure during low tide (Figure 2b) and high tide (Figure 2c), as well as their water level record for the
acquisition period of the satellite images (Figure 2d).



155

Figure 2: The location of the four New Zealand estuaries where the SDT method was tested (a). Tauranga Harbour and tide gauge locations during low tide (b) and high tide (c) with the background image from ESA Sentinel 2A. Water level time series from the three of local tide gauges shown in panels b and c during the period over which satellite images were acquired (d). The water levels associated with images shown in panels b and c are marked with yellow and red symbols (Vertical Datum: MSL).

160 2.2 Satellite-derived topography: the waterline method.

Our proposed framework to generate the SDT in intertidal zones using the waterline method (waterline-SDT) is composed of four stages, as illustrated in Figure 3: stage 1 is to query an image collection, stage 2 is to identify the intertidal zone, stage 3 is to determine the waterline position and height, and stage 4 is to post-process results. First, we acquired an image collection for each estuary through the Google Earth Engine application (Gorelick et al., 2017) using the Google Colaboratory environment. Each image collection has images from the satellite Sentinel 2A and B, product type level-2A, covering the estuary domain, in which less than 5% of the pixels are covered by clouds. We have allowed a certain number of images with low cloud coverage because of the restricted number of available images; however, any irregularities from the small areas of clouds and their shadows were removed manually in the post-process analysis. The number of images corresponding to the collection and environmental properties for each estuary (e.g., coverage of intertidal zone in the estuary; spring tidal range) is shown in Table 1.

170

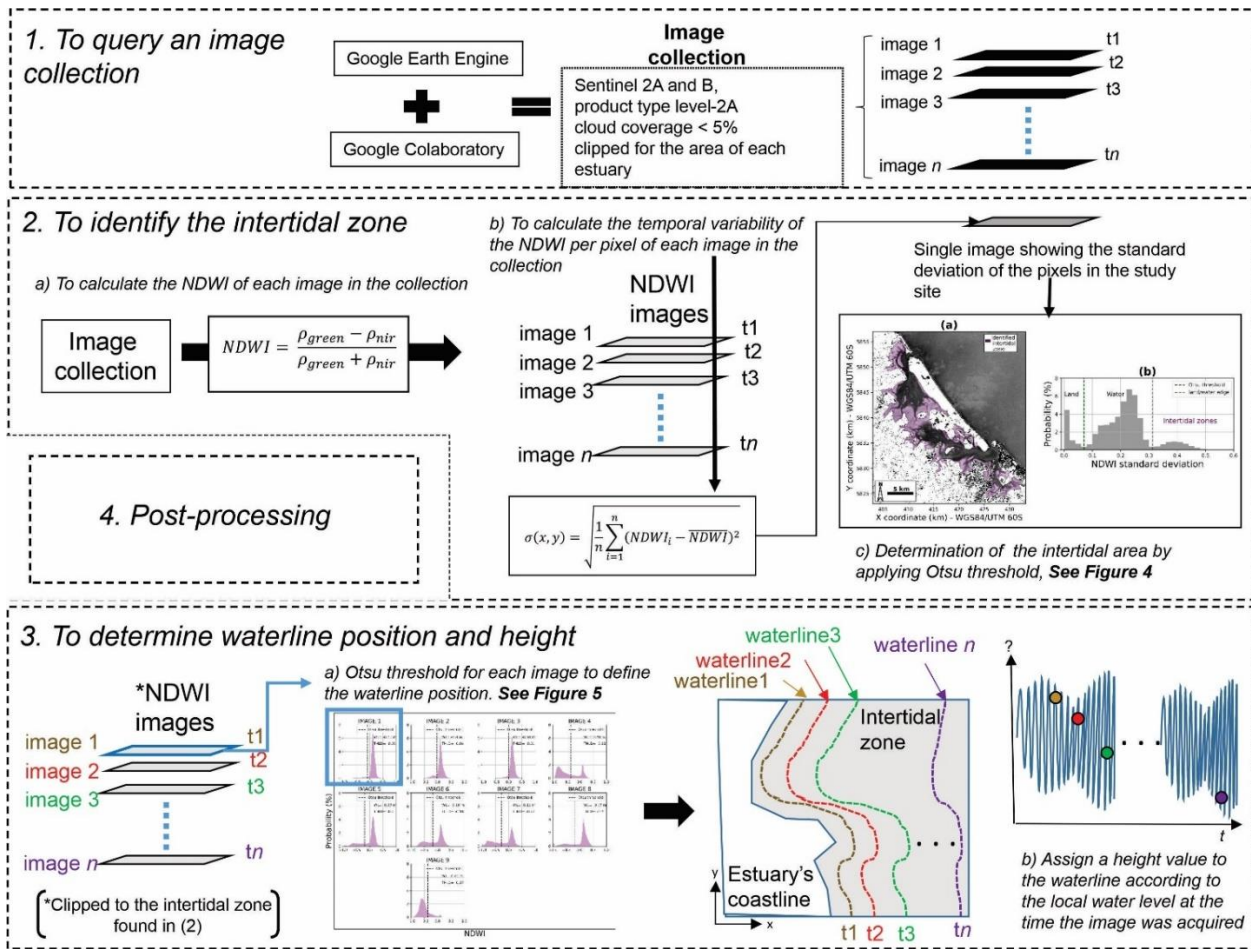


Figure 3: Our proposed framework for application of the waterline method to derive topographic data in intertidal zones. NDWI is the index used to detect the existence of water from satellite reflectance (see text).

175

Table 1 Number of images in the image collection for each estuary.

Estuary	<i>N^o</i> of images in the collection	Total intertidal area (Hume et al., 2016)	Surface area (Hume et al., 2016)	Spring tidal range
Tauranga Harbour	9	77%	~200.44 km ²	1.75 m
Ōhiwa	6	84%	~27.00 km ²	1.9 m
Maketū	12	58%	~ 2.64 km ²	1.4 m
Whitianga	8	72%	~ 15.50 km ²	1.7 m

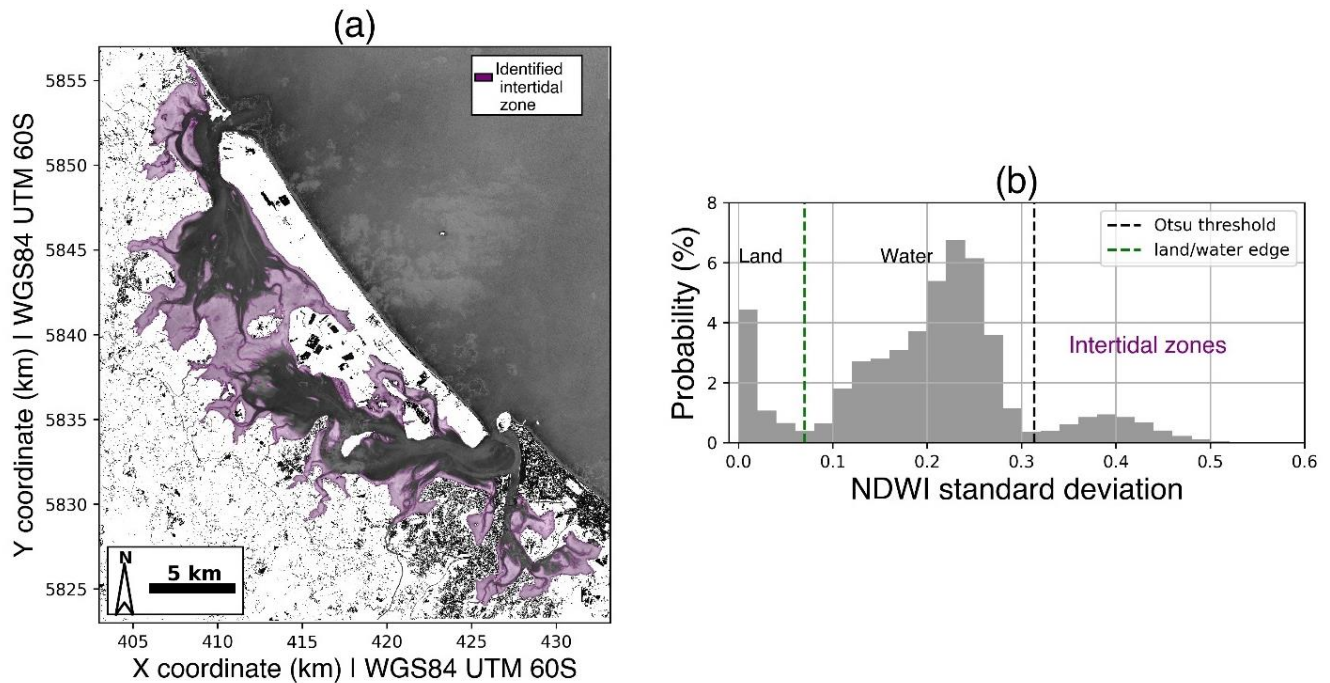
To eliminate pixels that are not in the intertidal area (stage 2 in Figure 3) — thus avoiding needless image processing — we used the approach based on Bué et al. (2020). We identify the intertidal zone by calculating the temporal variability at each pixel of the Normalized Difference Water Index (NDWI) (McFeeters, 1996) over the entire image collection, using Equation 1:

$$\sigma(x, y) = \sqrt{\frac{1}{n} \sum_{i=1}^n (NDWI_i - \overline{NDWI})^2}; \quad (1)$$
$$NDWI = \frac{\rho_{green} - \rho_{nir}}{\rho_{green} + \rho_{nir}};$$

185

where x and y are the pixel coordinates, n is the number of images in the collection, ρ_{green} and ρ_{nir} are the reflectance of the green and near-infrared bands of Sentinel-2 images, respectively. As a result, one single grey scale image is generated representing the $NDWI$ temporal standard deviation (σ), Figure 4(a). Because of the consistent change between exposed (low tide) and inundated (high tide) conditions, we assume that the highest standard deviation values will occur in the intertidal zones. Thus, we determine that the pixels representing the intertidal zone are the ones with an σ greater than a threshold value — for Tauranga Harbour, the threshold is > 0.32 , Figure 4(b). The threshold is set using the Otsu approach (Otsu, 1979), where its value depends on the probability distribution of σ in each image. The Otsu method identifies the optimum threshold between two data classes in the image distribution that maximizes the value of the within-class variance. The advantage of using an adaptive threshold is that we can objectively tailor the threshold to each image collection and estuary.

190



195

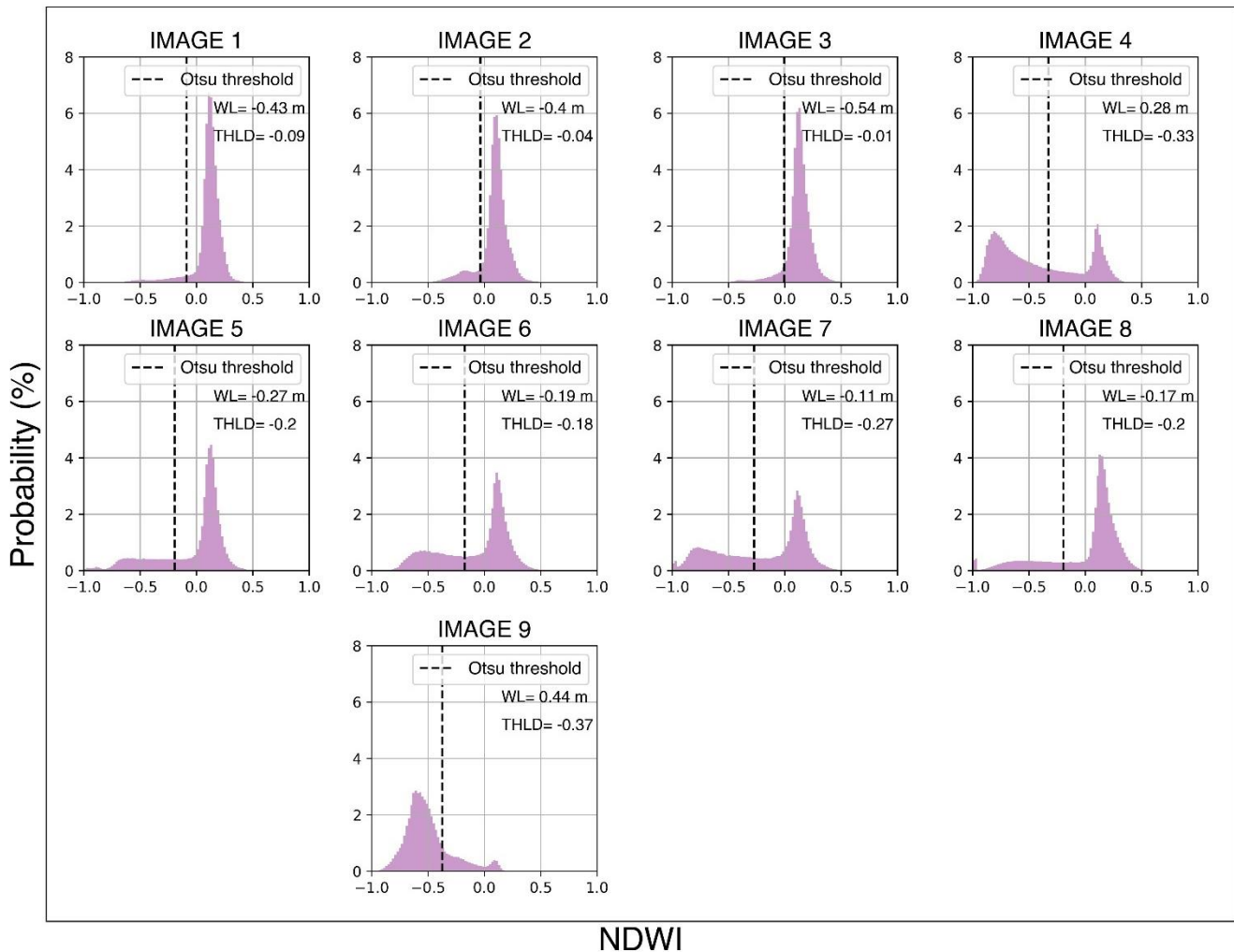
Figure 4: (a) Intertidal areas identified using the temporal variability of *NDWI* of the Tauranga Harbour image collection. Determination of the Otsu threshold for the identification of the intertidal zone (b).

In the third stage (Figure 3) for each image in the collection, we clipped the corresponding *NDWI* maps into the intertidal zone (which was defined using the whole image collection in stage two). From the intertidal *NDWI* maps, the waterline position in that image was extracted by applying the algorithm “Finding_Contours” from the scikit.measure (Van DerWalt et al., 2014) Python library. This contour extraction method searches for a given value (threshold) in a two-dimensional array of pixels, using the ‘marching squares’ algorithm (Lorenzen and Cline, 1987) to precisely identify contour boundaries by linearly interpolating between adjacent pixel values; therefore, the method is able to define waterline with a subpixel resolution. We used Otsu method to determine the threshold that should be applied to each image; Figure 5 shows the distribution of *NDWI* for each image in the Tauranga collection. Once we identify the waterline for a given image, we assign a height value to it by finding the corresponding observed tide level at the local tide gauge (Ōmokoroa for the Tauranga Harbour case study, Figure 2D). After we have processed all images in the collection, several waterlines with different height values are created (see Figure 3, stage 3b), which can be gridded to create the waterline-derived-STD (hereafter the “waterline-STD”). We assessed the accuracy of the STD against the LiDAR data by comparing the waterline sample-by-sample and the corresponding digital elevation model (DEM). We used the module DELFT-QUICKIN to create DEMs for each estuary. The triangular interpolation method was applied in a grid with a spatial resolution of 10 m.

200

205

210



215 **Figure 5: Otsu threshold (THLD) applied to identify the waterline position for each image in the Tauranga Harbour collection. The observed water level from the Ōmokoroa tide gauge at the moment of the image acquisition (i.e., waterline height relative to mean sea level) is also shown in each panel (marked WL).**

2.3 Satellite-derived bathymetry: the ratio-log method.

220 Additionally, the ratio-log method (Stumpf et al., 2003) was applied in Tauranga Harbour separately for intertidal zones (ratio-log-SDT) and shallow water (ratio-log-SDB) (the ratio-log-SDT is used in the comparison of methods in Part (a), Figure 1 and both the SDT/SDB are used in the assessment of modelling in Part (b), Figure 1). Originally, the ratio-log empirical approach has been used to derive shallow water bathymetry. However, because of the relative low turbidity of intertidal water in Tauranga Harbour, we hypothesized that the method could be suitable also for deriving topography on intertidal zones. We applied the method to an image acquired at high tide, where the intertidal zone was completely flooded.

In the Part 2 of the study, we use the SDT and SDB in the hydrodynamic modelling (building on a pilot study in Costa et al. (2021)), where the method was trialled in a sub-estuary of Tauranga Harbour). Detailed information about the application of the ratio-log method and the results for tidal flats and shallow water are provided in Supplement A, Figure S1 and Figure S2. Because the method is based on an empirical fit, additional bathymetric data are needed to implement the ratio-log method for shallow water. For this, we used the multiple-source bathymetric data detailed in Sect. 2.4.

2.4 Hydrodynamic modelling: the baseline model

A baseline hydrodynamic model was set up for Tauranga Harbour. We only applied the modelling study to this estuary because it has already a previous model calibrated and validated for the bed roughness (following Stewart (2021)). The purpose of the baseline model was first to correct the waterline-SDT by accounting for the tidal propagation within the estuary (Sect. 2.5.2); the second was to assess the use of SDT and SDB as a boundary condition in modelling extreme water levels in estuaries (Sect. 2.6). We used the model DELFT3D-FLOW for this task. The grid domain and interpolated bathymetry are shown in Figure S4 (Supplement B), and they cover the central to the southern part of the Harbour with a 20×20 m resolution grid. We set the north and south boundaries as open boundaries (free Neuman), and we forced the water level along the seaward boundary with the astronomical components of the tide. For the latter, harmonic astronomical tidal analysis was undertaken on the Moturiki Island tide gauge using U_tide (Codiga, 2011). The topographic and bathymetric data used in the hydrodynamic model were assembled using a combination of data from multiple sources: Multibeam survey (Port of Tauranga, 2017), LiDAR (2008 from AAMHATCH and 2016 from LINZ) and LINZ hydrological charts NZ 5411, 2016. These data were all converted to mean sea level (MSL) vertical reference.

The model was validated to ensure the bed roughness parameters were appropriate by simulating an equinoctial tidal period from 01/03/2019 to 31/03/2019. The details of the model setup, calibration and validation are presented in Supplement B. The vertical datum in the simulation was the MSL, and the time step was 0.5 min; the advection scheme for calculating the flooded and dried cells is cyclic, using the water level averaged on the grid cells. We calibrated the model against three tide gauge observation points (Ōmokoroa, Hairini and Ōruamatua). The model approximates the predicted data well (shown in Supplement B).

2.5 The SDT correction approaches

2.5.1 Correcting SDT using the bias between LiDAR data and SDT: the statistical correction

The accuracy of the waterline SDT method can be limited by environmental conditions that affect the ability to correctly determine the waterline at different tide levels within the tidal flats and at the boundary between shallow water and intertidal zones. — e.g., the complexity of the intertidal zone morphology, water turbidity and variation of the benthic substrates. All estuaries that we studied have similar environmental conditions; for example, the complexity of the morphology (they are all

255 barrier-enclosed estuaries with channelization), the white-sand substrate, the presence of seagrass, and the groundwater seepage can be potential sources of error in topographic data estimates. Groundwater seepage leaves a film of moisture on the exposed intertidal detectable in images (Huisman et al., 2011). Therefore, a statistical correction was developed on the basis that the detected waterline is consistently further seaward or landward than the actual waterline because of these environmental conditions. For the statistical correction, we fitted a linear equation between the value of the Otsu threshold — used to
260 positioning the waterline within the intertidal zone (see Sect. 2.2) — and the bias between the waterline-SDT and the LiDAR data in all the estuaries we studied. The statistical correction removed the bias.

2.5.2 Correcting SDT using hydrodynamic model: the dynamical correction

When a tidal wave propagates inside an estuary, it can experience wave deformation such as shoaling, reflection and dampening, which implies, together with the time it takes for the tide to propagate around a large estuary, that the water level
265 is not homogeneous throughout the estuary at one instant in time. Thus, when considering a water level recorded in a single tide gauge to assign height values to a waterline, our estimates can be higher or lower than the actual waterline elevation. To correct the waterline-SDT (Sect. 2.2) for the tidal propagation, we used a hydrodynamic model (Sect. 2.4); this correction approach is hereafter called dynamical correction, and we implemented it as follows.

270 First, we replace the model bathymetry in the intertidal zones with the statistically-corrected waterline-SDT. We retained the original bathymetry in the shallow water areas and created a new depth file. Using this new depth file, we performed nine independent simulation cases corresponding to the nine images in the Tauranga image collection. Each case had a simulation period corresponding to the ten days prior to the date and time that the satellite image was acquired to ensure that initial conditions were no longer important. We then associated each of the spatially-varying waterlines (determined as described in
275 Sect. 2.1) with the corresponding spatially-varying water level model output, using interpolation to extract collocated water levels from the gridded model output. As a result, the water levels of each waterline extracted from each image varied spatially rather than set to a constant — as is the case of the waterline-SDT derived according to Sect. 2.2.

2.6 Assessing water level simulations with SDB and SDT

We developed four different simulation scenarios to evaluate the accuracy of hydrodynamic simulations using SDB and SDT
280 against the use of our existing model bathymetry which was created with LiDAR, multibeam and echo-sounder data (‘surveyed bathymetry’ in Table 2). The latter is our baseline model, S1, and was described in Sect. 2.4. The S1 scenario simulates when the modeller depends only on the in situ measured bathymetry. In the S2 and S3 scenarios, we replaced the intertidal zone bathymetry with the SDT generated by using the waterline (waterline-SDT) and the ratio-log (ratio-log-SDT) methods, respectively. The S4 scenario was developed to assess the use of only SDB and SDT in the entire model domain (so only
285 satellite-derived data). We use the waterline-SDT in the tidal flat and the ratio-log-SDB for the shallow areas within the harbour. To assess the simulations, we compared the water level prediction made by each scenario against water level observations at

the three points (Ōmokoroa, Hairini, and Ōruamatua) and the water level output maps from each simulated scenario in terms of RMSE, MAXE, and R2. Other configurations applied to the scenarios (i.e., time period, time step, forcing conditions) are the same as described in Sect. 2.4.

290

Table 2 - Simulation scenarios to assess the use of SDT and SDB in hydrodynamic modelling.

Scenarios	Source intertidal zone	Source shallow waters
S1	surveyed bathymetry	surveyed bathymetry
S2	waterline-SDT	surveyed bathymetry
S3	ratio-log-SDT	surveyed bathymetry
S4	waterline-SDT	Ratio-log-SDB

2.7 Assessment of framework performance

We assessed the accuracy of the SDB, SDT, the hydrodynamic model, and the dynamical and statistical corrections by calculating the following error metrics: root mean square error (RMSE), maximum absolute error (MAXE), relative error (RE), coefficient correlation (R2), and bias (BIAS) (Eq. 3–7 respectively). In the corresponding equations, h_{est} is the estimated value (e.g., SDT, SDB, hydrodynamic model output), and h_{obs} is the observed value (e.g., LiDAR data, tide gauge measurements). In the case of SDB and SDT evaluation, its relative error can be either negative or positive when the SDB/SDT is shallower or deeper than the LiDAR or surveyed data, respectively. For illustrating this calculation, a schematic is provided in Figure 6, showing that although the error is evaluated in height differences, it can arise because of either horizontal or vertical inaccuracies.

300

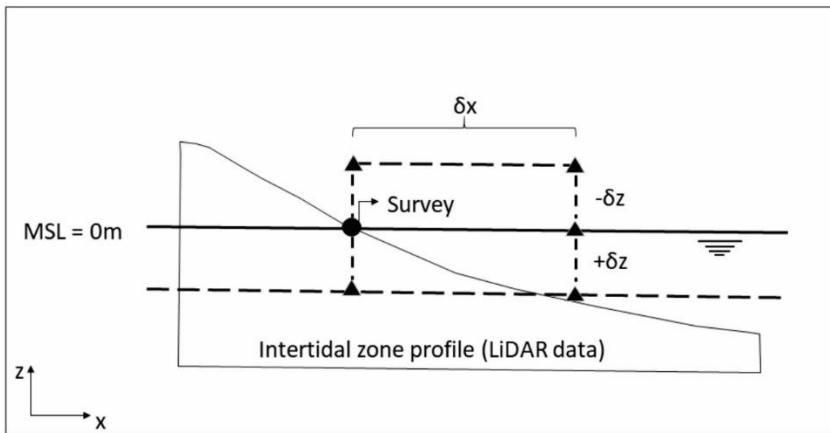
$$RMSE = \sqrt{\frac{\sum_{i=1}^n (h_{est_i} - h_{obs_i})^2}{n}}; \quad (3)$$

$$MAXE = \max_{i=1 \dots n} |h_{est_i} - h_{obs_i}|; \quad (4)$$

$$RE = h_{obs} - h_{est}; \quad (5)$$

$$R^2 = \frac{\sum_{i=1}^n (h_{est_i} - \overline{h_{obs}})^2}{\sum_{i=1}^n (h_{obs_i} - h_{est_i})^2 + (h_{est_i} - \overline{h_{obs}})^2}; \quad (6)$$

$$BIAS = \overline{h_{obs}} - \overline{h_{est}}; \quad (7)$$



310 **Figure 6:** Schematic showing the error calculation. The circle shows the actual location of the water line, and triangles show the location of the remotely sensed shoreline. There are two ways that an error can be caused. The waterline can be detected landward or seaward of its actual location (δx), or the waterline is assigned an elevation that is too high or too low (δz).

3 Results

3.1 The waterline satellite derived topography (waterline-SDT)

315 The waterline-SDT accuracy, compared to the LiDAR data, for all the studied estuaries, is shown in Table 3; the average RMSE across all estuaries was 0.33 m, and the average MAXE was 1.74 m. The technique's worst performance was in the Maketū estuary (RMSE = 0.41 m and MAXE = 2.38 m), Figure S6. Ōhiwa and Whitianga estuary have similar performances, Figure S5 and S7. Tauranga Harbour is associated with the best estimates with RMSE = 0.20 m. Note that the error parameters calculated for the corresponding DEMs show lower errors, especially in terms of MAXE. The details about the images that
 320 were acquired and the corresponding water level for each estuary is shown in Supplement C.

Table 3 Waterline-SDT errors for every studied estuary. DEM is the digital elevation model obtained by interpolating the corresponding waterline-SDT in the intertidal zone with spatial resolution of 20m and triangulation method. The elevation range in the LiDAR data within the intertidal zone is also shown. Vertical Datum: MSL.

<i>Estuary</i>	<i>SDT</i>		<i>DEM</i>		<i>LiDAR</i>
	<i>RMSE (m)</i>	<i>MAXE (m)</i>	<i>RMSE (m)</i>	<i>MAXE (m)</i>	<i>elevation range (m)</i>
<i>Maketū</i>	0.41	2.38	0.47	2.19	-0.63 +1.90
<i>Ōhiwa</i>	0.35	2.00	0.34	1.61	-0.98 +2.98
<i>Tauranga Harbour</i>	0.20	1.60	0.23	1.14	-1.11 +1.44
<i>Whitianga</i>	0.35	1.00	0.28	1.17	-1.12 +1.92
<i>Average</i>	0.33	1.74	0.33	1.53	

Although the SDT accuracy differs depending on the estuary, we observed that the MRE increases at high and low tide for all estuaries, and the lowest errors occur at mid tide. We found a linear correlation between the mean relative error (MRE), the waterline height (Z), and the Otsu adaptive threshold (THLD), which also demonstrates the aforementioned tide-level dependency. For instance, we found that the THLD and the MRE are correlated by $R^2 = 0.58$ (Figure 7b); The THLD and the Z by $R^2 = 0.82$ (Figure 7a), and MRE and Z by $R^2 = 0.68$ (Figure 7c). However, whether a water is collected on the flooding or the ebbing tide cycles do not affect the waterline-SDT accuracy. Equation 8 (Figure 6c) is then applied to remove the statistical bias in the waterline-SDT for Tauranga Harbour, which we refer to as the statistical correction (Sect. 2.4.1).

335
$$\text{MRE} = -0.492 * Z - 0.089 \quad (8)$$

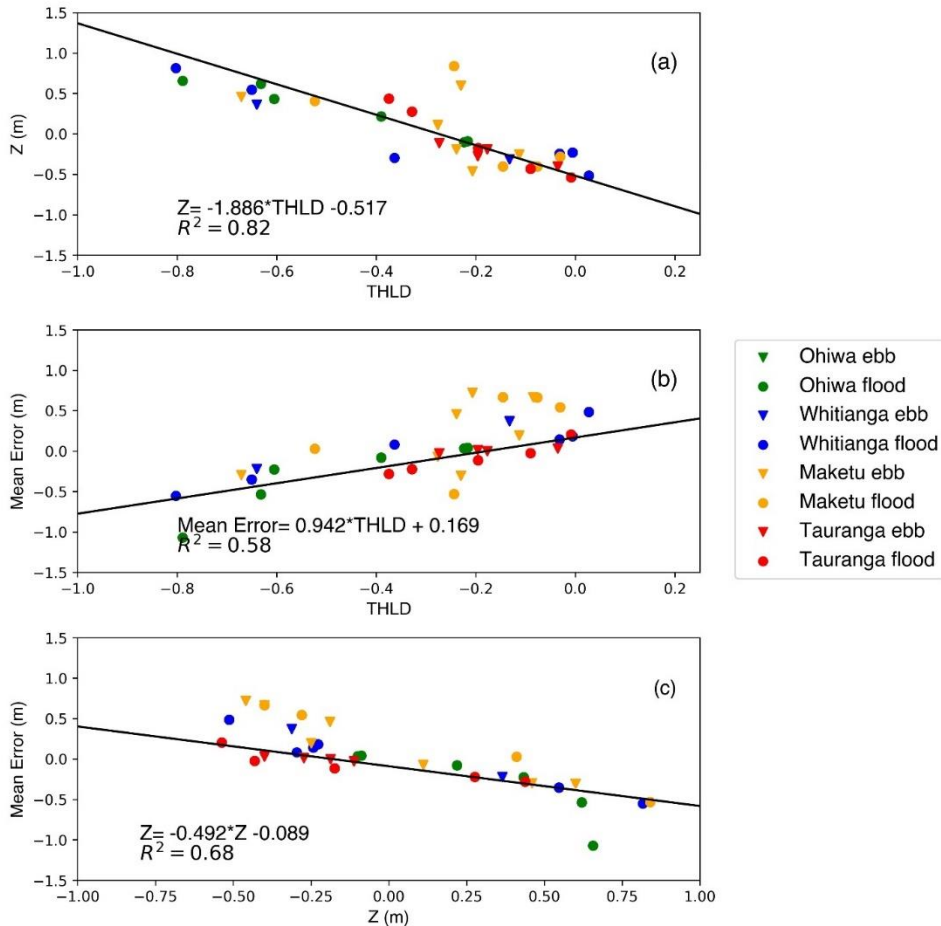
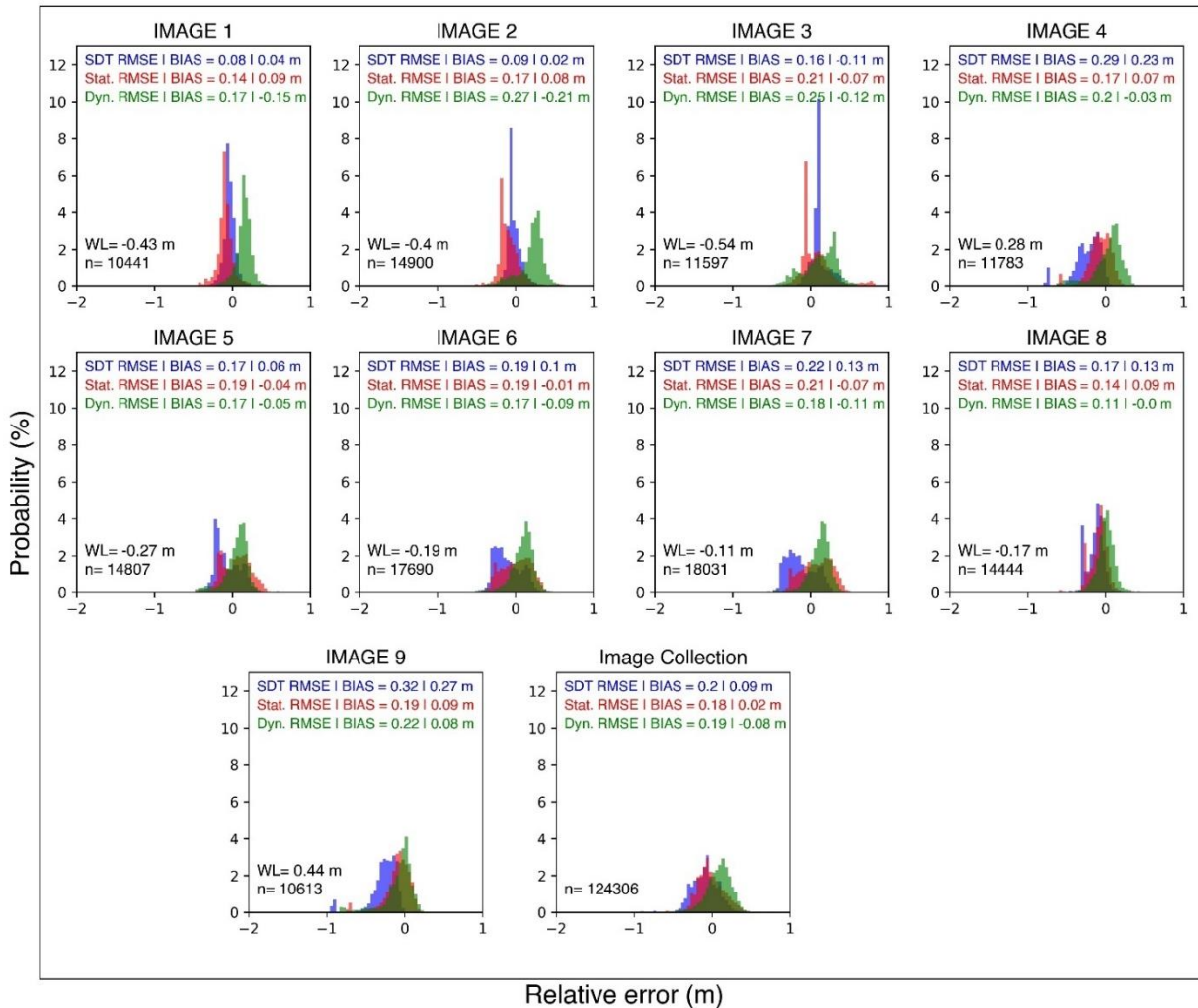


Figure 7: Statistical relationships at all estuaries (Ōhiwa, Whitianga, Tauranga, Maketū): (a) water level Otsu threshold (THLD) and observed water level (Z); (b) THLD and the SDB mean relative error per image; (c) Z and the SDB mean relative error per image R^2 .

340 **3.3 The statistical and dynamical corrections**

The waterline-SDT (Sect. 2.2), the statistically (Sect. 2.4.1 and 3.1), and the dynamically (Sect. 2.4.2) corrected waterline-SDT showed an overall RMSE equal to 20, 18 and 19 cm, respectively (Figure 8). The statistical correction is effective where the SDT is strongly biased (e.g., Figure 8, images 4 and 9). However, for the cases where the uncorrected SDT shows good results (Figure 8, images 1–3), the statistical correction worsens the bathymetric estimates by increasing the corresponding
 345 bias. The dynamical correction is more effective when the waterline is extracted from images collected at mid to high tides (Figure 8; images 4–9) than at low tides (Figure 8; images 1–3), improving the RMSE values by 5 cm on average. However, the estimates can worsen during low tides by 10.5 cm on average.



350 **Figure 8: Histograms of the waterline-derived SDT relative error (RE) for each image in the collection for Tauranga Harbour: waterline-SDT (blue), statistically corrected waterline-SDT (red) and dynamically corrected waterline-SDT (green). RMSE, BIAS, waterline height (WL), and number of waterline samples (n) are shown.**

3.4 Prediction of water level using the SDB

The simulation scenarios showed that the combined use of SDB and SDT can obtain similar or better water level predictions compared to those predicted using only surveyed bathymetry (although the log-ratio method requires some in situ calibration data). Figure 10 illustrates the average error parameters calculated when comparing the model output with the record of the three tide gauges. For a detailed assessment of each one of the gauges, please consult Supplement D. In S4, the waterline-SDT for intertidal zones combined with the ratio-log-SDB for shallow waters can predict the astronomical tide more accurately (RMSE~7cm; MAXE~25cm). In the S1 results, the model uses surveyed bathymetry (S1) with poorer performance (RMSE~9cm; MAXE~32cm). Specifically, at the location of the Ōruamatua tide gauge, the predictions were improved in the S4 scenario (RMSE=5cm; MAXE=17cm) compared to S1 (RMSE=13cm; MAXE=42cm), see Figure S9, Supplement D.

Regarding the scenarios where SDTs replace just the intertidal topography, S2 (waterline-SDT) provided superior performance (RMSE=7.4 cm, MAXE=24.3 cm, R2=0.97). In S3, the model uses ratio-log-SDT and shows poorer performance (RMSE=9.7 cm, MAXE=29 cm, R2=0.96).

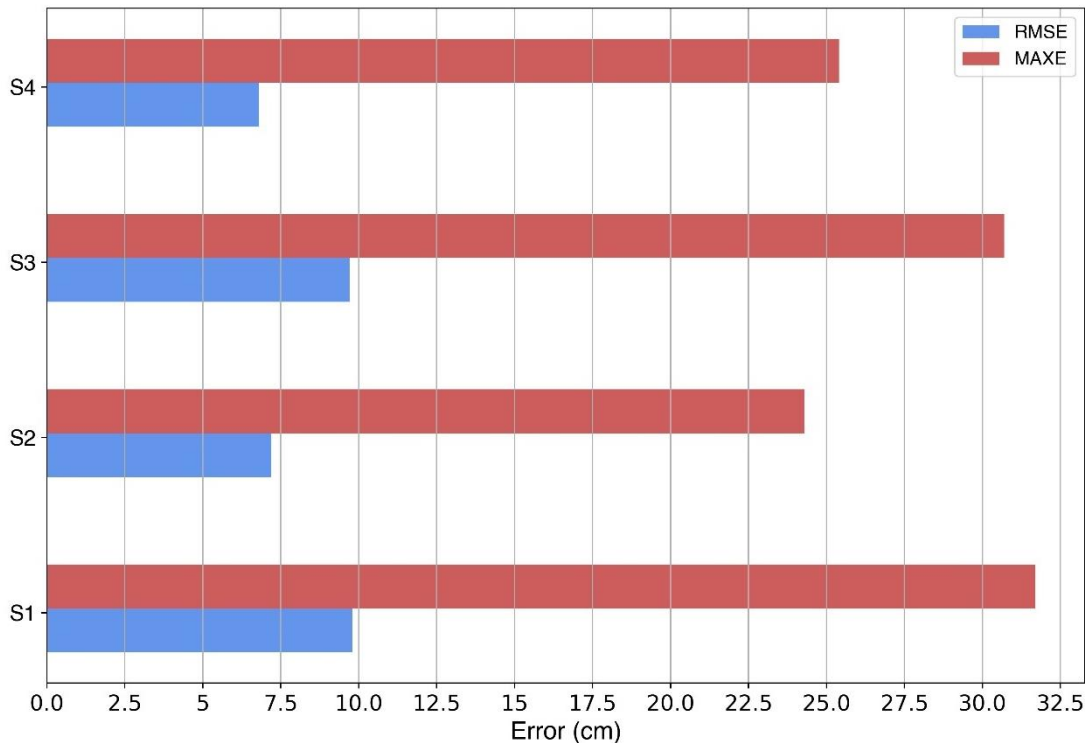
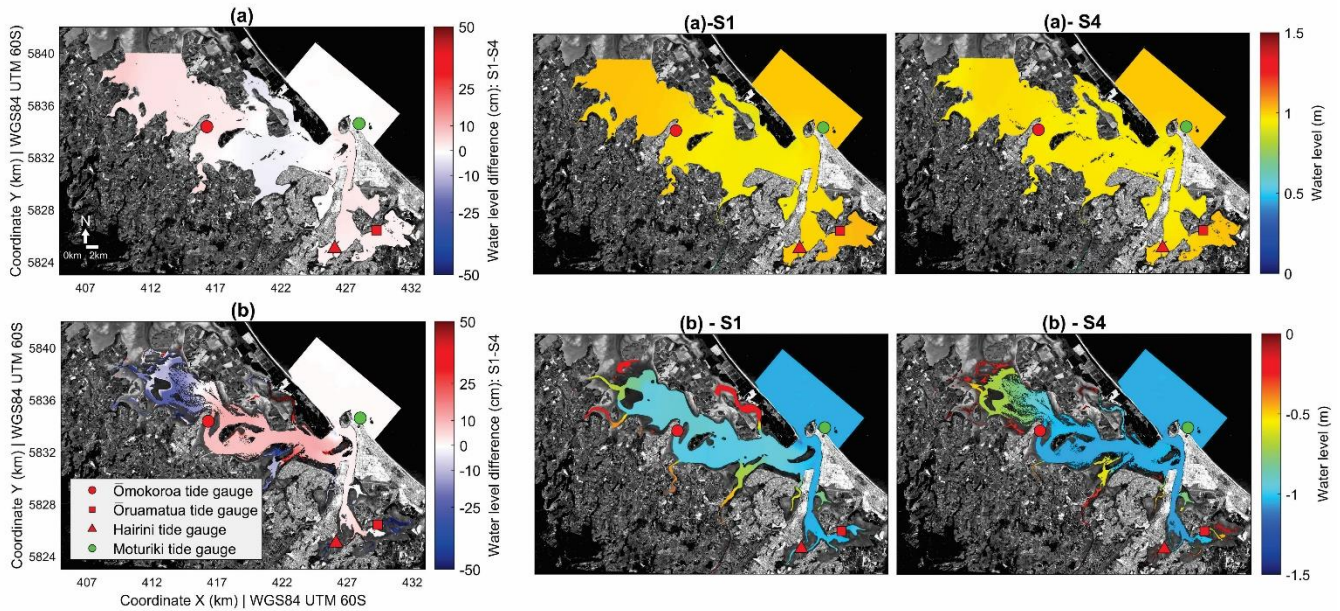


Figure 9: The average parameter errors calculated considering the results at the 3 tide gauge locations (Ōmokoroa, Hairini, Ōruamatua) for each simulation scenarios (S1, S2, S3, and S4) — RMSE (blue bar), MAXE (red bar).

The good agreement between scenarios S1 and S4 in Ōmokoroa, Hairini, and Ōruamatua can also be extended to the entire model domain. For instance, the difference between S1 and S4 is close to zero at the maximum water level in each grid cell

over the entire simulation (Figure 10, panel a). However, major differences in the water level predictions occur in the estuary's inner channels at the minimum (low-tide) water level at each grid cell (Figure 10, panel b).



375 **Figure 10: Spatial difference between the hydrodynamic model output using survey bathymetry (S1) and the waterline-derived plus ratio-log derived SDB (S4). High (a) and low tide condition (b), where positive means that the water level S1 is higher than S4. Background image: ESA Sentinel 2A. Date and time of the image acquisition: 18/12/2018 10:15 h.**

4. Discussion

We proposed a semi-automated framework to derive bathymetry and topography from satellite images by applying two well-known methods: the waterline method for elevation data in intertidal zones (e.g., Khan et al., 2019; Fitton et al., 2021; Jia et al., 2021) and the ratio-log empirical method for shallow waters (Stumpf et al. 2003). We combined the satellite-derived elevation techniques with cloud computation and database, allowing us to rapidly estimate topographic and bathymetric data for several locations simultaneously on a regional and large-scale (also shown in Jia et al., 2021; Fitton et al., 2021; Traganos et al., 2018). Here we focused on using these combined technologies for the hydrodynamic modelling of extreme water levels (caused by surges and tides) in enclosed estuaries. Our work adds to growing body of work on applying satellite techniques as an alternative to monitoring the coastline (Turner et al., 2021).

385

Our discussion is presented in four parts. In the three first parts, we addressed our first and second specific objectives, discussing our main findings and limitations when applying the waterline and ratio-log methods, including suggestion for improvements. In the fourth part, we addressed our third objective, discussing the challenges of using SDTs and SDBs in modelling extreme water levels within a complex-morphology estuary.

390

4.1 Our proposed waterline method for deriving topography from space-borne images and its limitations.

The waterline method compares well to LiDAR data in our study sites — considering that the topography in the intertidal zone ranges between -1.12 m to +2.98 m relative to MSL (see Table 3), and the vertical and horizontal accuracy of the LiDAR data are 20 cm and 60 cm, respectively. Although it is hard to directly compare different studies because they are conducted in different coastal areas, our results show a similar bias to other studies performed in similar estuarine environments. For instance, Salameh et al. (2020), applied the waterline method to Arcachon Bay in France, with the estimated DEM accuracy of RMSE = 0.27 m; Bué et al. (2020) generated SDTs for Azinheira estuary (Portugal) based on logistic regression with an RMSE = 0.6 m.

Despite the good results of waterline-SDT in NZ estuaries, the method is sensitive to the correct positioning and height-assigning of the waterline. Our results also shows that environmental conditions such as the complex morphology, varied bed substrates, and groundwater seepage could reduce the accuracy of the waterline position. Also, the location of the tide gauge used to assign the waterline height is important. For instance, Maketū estuary is a small estuary with complex morphology, and the tide gauge of Moturiki is located at approximately 27 km from the estuarine entrance, which likely explains the very low accuracy of SDT for that location. Furthermore, using just one tide gauge to assign the waterline height can add vertical error to the estimates because it does not account for the tide deformation and propagation in such a complex environment. Maketū is also undergoing staged engineering works to remove former flood protection which could have caused changes to the bathymetry between images and after the LiDAR survey was undertaken.

Complex morphology affects the estimates differently over different parts of the topographic profile — waterlines closer to the MSL (water level ~0 m) are more accurate, and waterlines closer to the peak of the high and low tides are less accurate (see Sect. 3.3). Our results corroborate those of Liu et al. (2013), who quantitatively analysed the waterline method in Dongsha Sandbank, China (an exposed coastal area). In their study, the authors have found that the main error source in the waterline method is linearly correlated to the slope and area of the intertidal zone. Furthermore, having enough images to characterise the morphology of the study site is also a limiting factor in the waterline method, as pointed out by several studies (Salameh et al., 2019; Liu et al., 2013). Our results are also clearly affected by the number of images in our collection. For instance, we observed gaps between different waterlines, where no topographic data could be derived, shown in Fig. 7 (Sect. 3.2). Although we have used Sentinel-2 images acquired every five days, they are often not useable due to cloud coverage.

The bed substrate can directly affect the waterline positioning, especially in New Zealand estuaries, where clear water is common. For instance, in Tauranga Harbour the seagrass banks, (Ha et al., 2020) and the groundwater seepage (shown to cause an error in water line detection in Huisman et al., 2011) can abruptly change the reflectance of the pixels around the waterline, especially in the centre part of the estuary, where the seagrass banks can be seen (Figure S3). We used the adaptive

Otsu method (Nobuyuki Otsu, 1979) to detect the edges between water and intertidal zones. The method showed good
425 performance for determining the waterline location in estuaries, corroborating studies on lakes, rivers, water reservoirs
(Donchyts et al., 2016), and coastlines (Vos et al., 2019). We have also tested the edge identification by calculating the mean
or the median of NDWI distribution following approaches in previous studies (Sagar et al., 2017; Bishop-Taylor et al., 2019),
but these did not performance as well (not shown). However, the Otsu method defines a threshold by detecting the value that
maximises the within-class variance between two classes of a grey-scale distribution, which can cause two limitations: first,
430 the inability to correctly detect waterlines in images with complex conditions, i.e., where the water is clear, and the bed
substrates reflectance can be seen in the satellite images; second, the Otsu threshold method will detect waterlines even when
all intertidal pixels are flooded or exposed, adding bias in the extremes of the topographical profiles (peak of high or low tide).

There are currently several methods for edge detection that have been implemented in waterline-SDT that can potentially
435 overcome the issues highlighted above. One practical solution would be the manual identification of the waterline; however,
it is subjective and labour-intensive when applied over a large area and in multiple study sites. Another way would be to apply
image segmentation techniques, for instance, K-means clustering techniques applied to edge detection (Salameh et al., 2020).
Alternatively, the simple identification of sea-grass banks could be used to remove areas where the waterline is poorly detected
prior to analysis. Ha et al. (2020) identified seagrass using ensemble-based machine learning algorithms. Caballero and Stumpf
440 (2020) identified algae and seagrass by using an empirical formula to calculate the maximum chlorophyll index, which uses
three different optical bands to explain the radiance peak at the red-edge band.

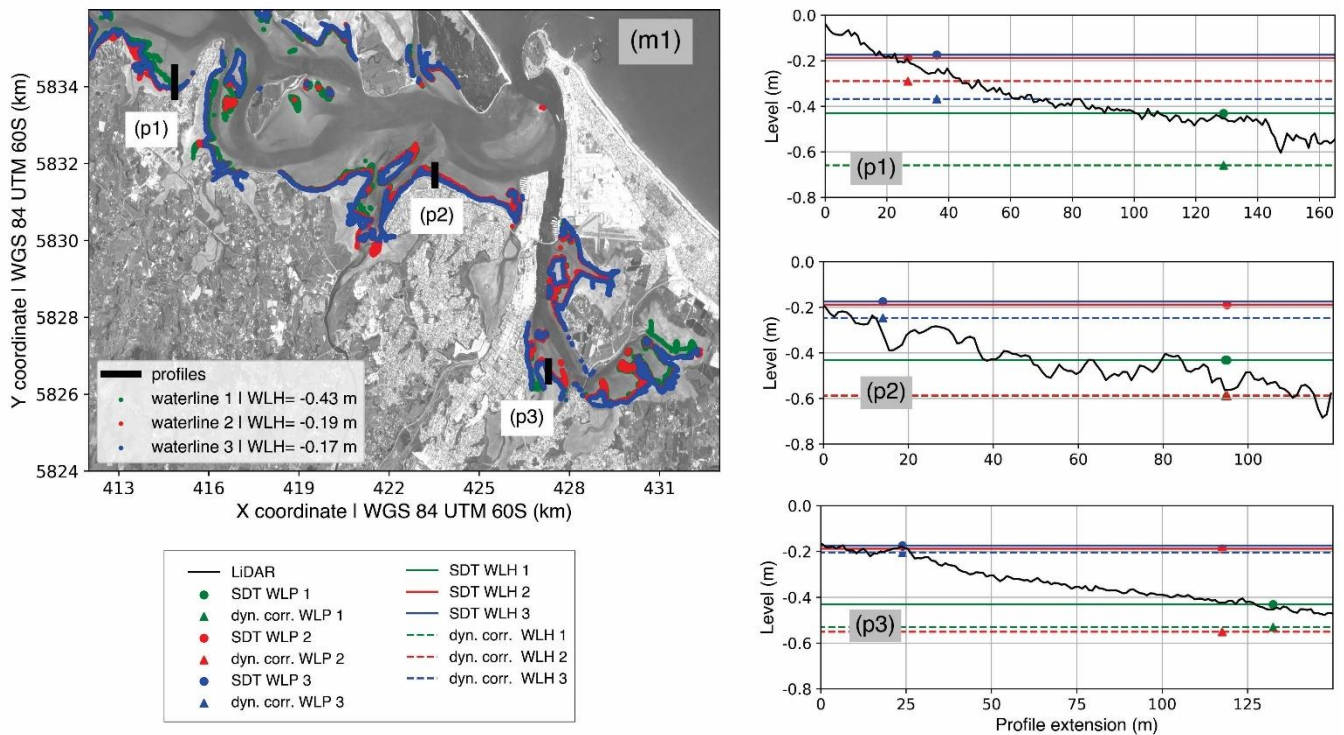
4.2 Our proposed correction methods for waterline-SDTs.

Our proposed correction methods (i.e., statistical and dynamical) for the SDT only resulted in a 1–2 cm improvement across
the case-study estuary. However, our insights into why and where the correction resulted in improvements provide the basis
445 for further work (e.g., when more imagery becomes available to test error sources more thoroughly). The statistical relationship
between the error and the waterline height, the elevation on the tidal flat (LiDAR) and the waterline detection threshold in all
four studied estuaries allowed us to set a semi-independent framework to correct the vertical level in the waterline derived
SDT. For instance, we can first learn the relation between THLD and MRE in similar estuaries. And then apply the correction
to an entirely different study area with similar intertidal zone properties. For instance, estuaries with similar sediment colour,
450 water turbidity, spring tidal range and intertidal area coverage.

The dynamical correction gives more realistic waterline heights because it accounts for the tide propagation within the estuary.
However, the approach did not significantly improve the SDT. We hypothesized three reasons for the limited improvement.
First, inaccuracies in horizontal waterline position may be more important than inaccuracies in the waterline height. When
455 correcting the waterline height (vertical errors), we are not eliminating the horizontal errors. Figure 11 shows three different
waterline positions along three different profiles. The uncorrected waterline-SDT is represented for three different waterline

positions (coloured circles: red, green, blue) with their corresponding heights (solid line). The corresponding dynamically corrected waterline position and height are plotted, represented by the triangles and dashed lines, respectively. In Figure 11, we observed that some of the dynamically corrected waterlines (i.e., coloured triangles) are further seaward or landward in the topographic profile from where they should be. For instance, all the corrected waterlines in P1 (i.e., red, green and blue triangles) should be further seaward than they are. In P2, the blue-triangle waterline should be slightly landwards, and the red- and green-triangle waterlines, further seaward. In P3, all corrected waterlines should be further seaward. However, when the waterline is well positioned, waterline heights can be closely corrected to the LiDAR data; for instance, in P2 for all waterlines (dashed lines); and in P3 for the red and blue dashed lines.

465



470

Figure 11: Profile analysis of the dynamical correction in three different profiles (p1, p2, p3). [m1] shows the location of the profiles in Tauranga Harbour. [p1, p2, p3] shows the waterline height (WLH) and position (WLP) of three different waterlines (green (1), red (2), blue (3)) derived from the waterline-STD (STD) and their corresponding dynamically corrected (dyn. corr.) WLH and WLP. The continuous black line is the LiDAR data along each profile. Background image: ESA Sentinel 2A. Date and time of the background image acquisition: 18/12/2018 10:15 h.

The second factor that can influence the correction's performance is the hydrodynamic model accuracy — especially at low tide, as can be seen in Figure 10. The spatial resolution of the numerical grid (20 m) can limit the model's ability to correctly solve the flooding and drying within grid cells around narrow channels, potentially adding horizontal bias to the waterline heights. Moreover, the third limiting factor is the LiDAR data horizontal and vertical accuracy, which limits the potential

475

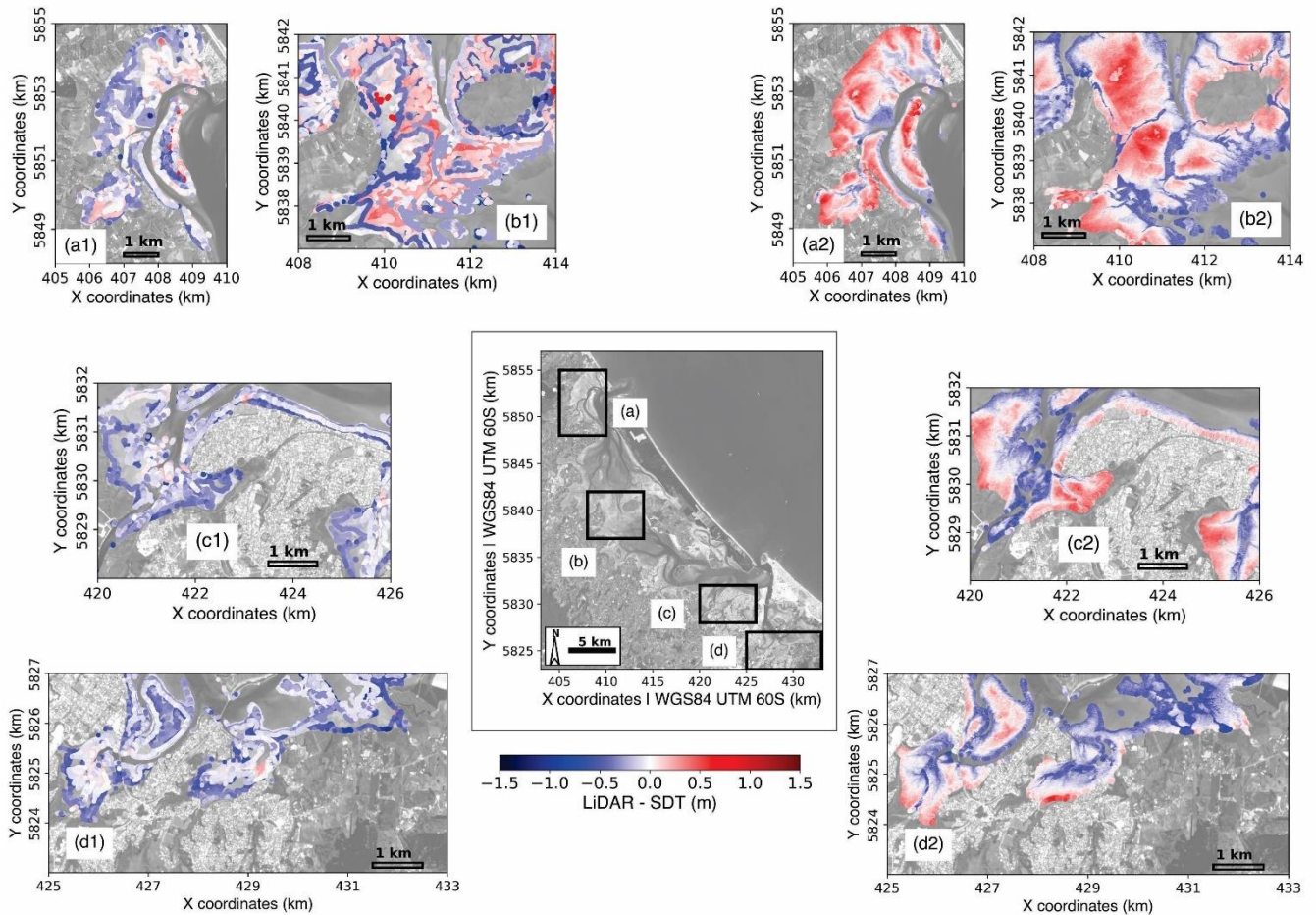
correction. The use of hydrodynamic modelling to assign the waterline heights is a common practice when generating SDTs (e.g., Liu et al., 2013; Khan et al., 2019; Salameh et al., 2020; Fitton et al., 2021). However, in most of the cases, the studies cover an extensive area, with exposed coastlines or sand banks, in which regional tide models are used where there are not
480 enough tide gauges to provide tide levels (Liu et al., 2013; Khan et al., 2019; Fitton et al., 2021). In just a few of these studies, enclosed estuaries were studied by setting up local-scale hydrodynamic modelling (e.g., Salameh et al., 2020; Liu et al., 2013).

For instance, in Arcachon bay (France), Salameh et al. (2020) compared the waterline-SDTs that were generated by assigning waterline heights according to single-location tide gauges, single-location model point output and grid hydrodynamic model
485 output. Similar to our results, they found that the waterline heights assigned by using grid model output did not improve the SDTs compared with using a single-location tide gauge within the estuary. They explained unexpected result as due to the slope of the tidal flat, and the model's inability to provide accurate sea level heights over the intertidal area. Similarly, Liu et al. (2013) used a regional tide model for the South Yellow Sea (China) to assign waterline heights to a local-scale study in Dongsha Sandbank (an exposed tidal flat), which limited the vertical accuracy of the SDT up to 30 cm (corresponding to the
490 model's accuracy).

4.3 Comparison between the waterline-method and ratio-log for intertidal zones.

Our results show that the waterline is a better method than the ratio-log for deriving topography using satellite images. The distribution of the relative vertical error (RE) of Tauranga Harbour's waterline-SDT and ratio-log-SDT for intertidal zones are shown in Figure 12. In the waterline-SDT (Figure 12 a1, b1, c1, and d1), the SDTs are generally shallower or further seaward
495 than the LiDAR — as the negative RE indicates (see Sect. 2.3) — with the worst estimates in the tidal flat's upper region (bluer colour dots). The positive RE values (redder colour dots) are concentrated in the estuary's wide flat centre region (Figure 12 b1) and indicate that the estimates are deeper or further landward than the LiDAR data.

The ratio-log-SDT (Figure 12: a2, b2, c2, d2) allows the water depth to be assessed on a pixel-by-pixel basis, with a resolution
500 of 10 m in the case of Sentinel Copernicus data; however, the associated error (RMSE=25 cm) is higher than the waterline-SDT (RMSE=20 cm). In the ratio-log-SDT, the intertidal zone becomes flat; the positive and negative errors are in the upper and lower parts of the tidal flats, respectively. In the middle of the topographic profile, the estimates are more accurate (whiter colour dots). The low data variability (pixels reflectance) probably causes the lower accuracy of the ratio-log-SDT in comparison to the waterline-SDT. The ratio-log (green/blue band ratio) poorly explains the depth (LiDAR data), which leads
505 to a low correlation coefficient ($R^2=0.12$). This assumption is confirmed by the higher correlation coefficient ($R^2=0.24$) obtained when the same method is applied to the shallow waters within Tauranga Harbour. In addition, the presence of seagrass in the intertidal zones and shallow water (Figure S3) can potentially worsen the ratio-log-SDT and SDB because it affects the reflectance of the pixel (Geyman and Maloof, 2019; Caballero and Stumpf, 2020).



510 **Figure 12: Estimated SDT and corresponding relative vertical error (RE) for intertidal zone in Tauranga Harbour using waterline-**
derived (a1, b1, c1, and d1 and ratio-log (a2, b2, c2, and d2) methods. Background image: ESA Sentinel 2A. Date and time of the
background image acquisition: 18/12/2018 10:15 h.

Numerous estuaries have turbid water, which would reduce the quality of SDBs and SDTs derived from both ratio-log and
 waterline methods. The ratio-log derivations would be affected by the interference of the suspended material on the light
 515 absorption rate through the water column — which could be improved by using methods that adjust the ratio-log method for
 turbid water (e.g., Caballero and Stumpf, 2020). The waterline derivations would be affected by intertidal zone identification.
 The NDWI of the pixels in shallow water with a high concentration of suspended materials could have similar values to those
 in the intertidal zone. Consequently, determining the intertidal areas would be more uncertain.

520 In addition, image pre- and post-processing are other factors that may improve the accuracy of the SDT and SDB of waterline
 and ratio-log methods. We used available Sentinel images already pre-processed by using Sen2Cor, which creates surface-
 reflectance images (see Sect. 2.1). However, several pre-processing tools are available (Pereira-Sandoval et al., 2019). Some

of these are designed specifically for use in coastal areas — where water is often turbid, containing a high concentration of suspended sediments and other materials. For instance, the ACOLITE tool (Vanhellemont and Ruddick, 2018) has been widely applied in estuaries (e.g., Bué et al., 2020; Salameh et al., 2020; Fitton et al., 2021). In the case of exposed coastal areas or where local wind waves can increase the rugosity of the water surface, filters to eliminate sun glint can be applied (Hedley et al., 2005)

4.4 Hydrodynamic modelling assessment

The bathymetric and topographic data quality is fundamental for reliable hydrodynamic modelling. Despite the limited accuracy of the SDT and SDB (see Sect. 4.1–4.3), our results show that hydrodynamic models using satellite-derived elevation can predict water level with similar accuracy in comparison with models using only surveyed data (see Sect. 3.4, Figure 11). Thus, we can infer that the water level modelling may not be sensitive to small uncertainties in the bathymetric data, but rather to the larger scale characteristics of the estuary, such as the width of entrances and overall geometry.

Some of the bathymetric uncertainties can arise from the interpolation technique used to create the DEMs (Circus et al., 2000; Kang et al., 2017, 2020; Salameh et al., 2020) — e.g., spline, kriging, inverse distance weighting (IDW), nearest neighbour, triangulation. However, previous studies have found that uncertainties in the elevation data lead to minor differences in the water level predictions (Cea and French, 2012; Falcão et al., 2013). For instance, Cea and French (2012) showed that water level predictions do not significantly change with vertical uncertainties of up to 1 m in the bathymetry. Similarly, Falcão et al. (2013) have shown that the DEMs created with the same interpolation technique (i.e., kriging) but with a different spatial resolution (i.e., 5 and 50m) did not significantly affect the water level prediction. Corroborating our results, Falcão et al. (2013) also found that the worst predictions are for grid cells where the water level is at a minimum, when comparing these two scenarios. The stream current magnitude and direction predictions are affected the most by the uncertainties in the bathymetric and topographic data (Cea and French, 2012; Falcão et al., 2013). In addition, bed roughness and eddy viscosity are two important calibration parameters highlighted in several studies (Pedrozo-Acuña et al., 2012; Mohammadian et al., 2022; Cea and French, 2012) that we have not explored in this manuscript because of its focus on SDT and SDB, although the parameters were calibrated for the hydrodynamic model.

Despite the uncertainties in the estimates, SDT and SDB can generate a fair approximation of estuary relief, which can be helpful in long-term predictions for coastal management applications. In idealistic numerical studies, the extension and slope of the intertidal zone, the estuary's length, and the width of the mouth are the main factors causing changes in the tidal range within harbours (Khojasteh et al., 2021; Du et al., 2018; Khojasteh et al., 2020). For instance, Du et al. (2018) show that the length of an estuary and intertidal zone slope strongly influences the tidal range. However, the entrance restriction drives the estuarine response to SLR (Khojasteh et al., 2020); the smaller the cross-sectional area of the estuary mouth, the smaller would be the tidal range within the estuary. Moreover, SDT and SDB could be used for data assimilation in numerical modelling, as

in Mason et al. (2010), who used the SDT to calibrate a morphodynamic model. Ultimately, the SDTs and SDBs can decrease the uncertainties of flood-risk management in the present and future scenarios of SLR where studies are limited due to lack of elevation data in remote areas such as small islands in developing states (Parodi et al., 2020) and coastal lagoons in developing countries (Pedrozo-Acuña et al., 2012).

560

Although the differences in the resulting water level between the SDT, SDB, and surveyed bathymetry simulation scenarios show that satellite techniques compare well, our simulations were only conducted in one estuary, albeit a large and relatively complex estuary — where the astronomical spring tides are the main driver for estuarine flooding. Therefore, studies are required in sites with different physical conditions would be useful to validate the use of SDT and SDB more broadly. For instance, estuaries where the storm surge is the main driver for flooding; or/and exposed estuaries where the wave forces can increase the water level (i.e., wave set-up) (e.g., Bertin et al. (2019)). Furthermore, modelling studies focusing on understanding whether or not the use of SDT and SDB properly represent the tide-surge interactions within the estuary are encouraged, due to the importance of the topic in water level modelling (Spicer et al., 2019; Wankang et al., 2019; Zheng et al., 2020), especially in the context of sea level rise.

565

570

5. Conclusions

A waterline technique for deriving topography from multispectral satellite images was developed and its use in hydrodynamic modelling assessed. The simple pre-processing required for the satellite images combined with the use of cloud computing and storage make the present framework highly applicable to regional scale studies. Our main findings show that the accuracy of the waterline SDT is similar or even superior to other techniques applied in previous studies to comparable sites, and similar to the vertical error in the LiDAR dataset used to assess accuracy. Statistical and dynamical corrections were trailed but provided limited improvements. The hydrodynamic modelling assessment was encouraging, and showed that SDT and SDB techniques have potential for use in high water level predictions (such as associated with higher than normal tides and storm surges). Scenarios using different applications of the SDT and SDB did not show major high tide differences over most of the numerical domain for Tauranga Harbour. The use of SDT and SDB for hydrodynamic modelling in estuaries can make flooding assessment for remote coastal areas feasible and provides a pathway around the need for expensive surveys for economically depressed vulnerable areas.

575

580

Code availability

The codes used in this work are available as python notebooks in <https://github.com/CostaAndCoasts/Intertidal-zones-satellite-derived-bathymetry>.

585 **Credit authorship contribution statement**

Wagner L.L. Costa: methodology, data analysis, writing – original draft, visualization. Karin R. Bryan: conceptualization, supervision, writing – review & editing, resources, funding acquisition. Giovanni Coco: Writing – review & editing, supervision.

Acknowledgment

590 The authors would like to thank Dr. Ben Stewart for numerical modelling assistance. This work was supported by the National Science Challenge: Resilience Challenge “Coasts” programme, GNS-RNC040. Data were supplied by Land Information New Zealand (LINZ), Bay of Plenty Regional Council, and Waikato Regional Council.

References

- Almeida, L. P., Efraim de Oliveira, I., Lyra, R., Scaranto Dazzi, R. L., Martins, V. G., andHenrique da Fontoura Klein, A.:
595 Coastal Analyst System from Space Imagery Engine (CASSIE): Shoreline management module, *Environ. Model. Softw.*, 140, 105033, <https://doi.org/10.1016/j.envsoft.2021.105033>, 2021.
- Ashphaq, M., Srivastava, P. K., andMitra, D.: Review of near-shore satellite derived bathymetry : Classification and account of five decades of coastal bathymetry research, *J. Ocean Eng. Sci.*, 6, 340–359, <https://doi.org/10.1016/j.joes.2021.02.006>, 2021.
- 600 Bertin, X., Mendes, D., Martins, K., Fortunato, A. B., andLavaud, L.: The Closure of a Shallow Tidal Inlet Promoted by Infragravity Waves, *Geophys. Res. Lett.*, 46, 6804–6810, <https://doi.org/10.1029/2019GL083527>, 2019.
- Bishop-Taylor, R., Sagar, S., Lymburner, L., andBeaman, R. J.: Between the tides: Modelling the elevation of Australia’s exposed intertidal zone at continental scale, *Estuar. Coast. Shelf Sci.*, 223, 115–128, <https://doi.org/10.1016/j.ecss.2019.03.006>, 2019.
- 605 Bué, I., Catalão, J., andSemedo, Á.: Intertidal bathymetry extraction with multispectral images: A logistic regression approach, *Remote Sens.*, 12, <https://doi.org/10.3390/RS12081311>, 2020.
- Caballero, I. andStumpf, R. P.: Retrieval of nearshore bathymetry from Sentinel-2A and 2B satellites in South Florida coastal waters, *Estuar. Coast. Shelf Sci.*, 226, 106277, <https://doi.org/10.1016/j.ecss.2019.106277>, 2019.
- Caballero, I. andStumpf, R. P.: Towards routine mapping of shallow bathymetry in environments with variable turbidity:
610 Contribution of sentinel-2A/B satellites mission, *Remote Sens.*, 12, <https://doi.org/10.3390/rs12030451>, 2020.
- Cea, L. andFrench, J. R.: Bathymetric error estimation for the calibration and validation of estuarine hydrodynamic models, *Estuar. Coast. Shelf Sci.*, 100, 124–132, <https://doi.org/10.1016/j.ecss.2012.01.004>, 2012.
- Circus, D., Kingdom, U., Extinction, M., andStrategies, S.: *M . D. Hylton 1 and M.B. Hare 1*, 6, 455–462, 2000.

- Codiga, D. L.: Unified Tidal Analysis and Prediction Using the UTide Matlab Functions, 59,
615 <https://doi.org/10.13140/RG.2.1.3761.2008>, 2011.
- Costa, W., Bryan, K. R., Coco, G., Zealand, N., and Zealand, N.: ASSESSING THE USE OF SATELLITE DERIVED BATHYMETRY IN ESTUARINE STORM SURGE MODELS – STUDY CASE : TAURANGA, 2021.
- Donchyts, G., Schellekens, J., Winsemius, H., Eisemann, E., and van de Giesen, N.: A 30 m resolution surface water mask including estimation of positional and thematic differences using Landsat 8, SRTM and OpenStreetMap: A case study in the
620 Murray-Darling basin, Australia, *Remote Sens.*, 8, <https://doi.org/10.3390/rs8050386>, 2016.
- Du, J., Shen, J., Zhang, Y. J., Ye, F., Liu, Z., Wang, Z., Wang, Y. P., Yu, X., Sisson, M., and Wang, H. V.: Tidal Response to Sea-Level Rise in Different Types of Estuaries: The Importance of Length, Bathymetry, and Geometry, *Geophys. Res. Lett.*, 45, 227–235, <https://doi.org/10.1002/2017GL075963>, 2018.
- Ehlers, J. S. and Rooney, J. J.: Depth Derivation Using Multispectral WorldView-2 Satellite Imagery, NOAA Tech. Memo.
625 NMFS-PIFSC-46, 24, <https://doi.org/10.7289/V5668B40>, 2015.
- Emanuel, K.: Increasing destructiveness of tropical cyclones over the past 30 years, *Nature*, 436, 686–688, <https://doi.org/10.1038/nature03906>, 2005.
- Falcão, A. P., Mazzolari, A., Gonçalves, A. B., Araújo, M. A. V. C., and Trigo-Teixeira, A.: Influence of elevation modelling on hydrodynamic simulations of a tidally-dominated estuary, *J. Hydrol.*, 497, 152–164,
630 <https://doi.org/10.1016/j.jhydrol.2013.05.045>, 2013.
- Fitton, J. M., Rennie, A. F., Hansom, J. D., and Muir, F. M. E.: Remotely sensed mapping of the intertidal zone: A Sentinel-2 and Google Earth Engine methodology, *Remote Sens. Appl. Soc. Environ.*, 22, 100499, <https://doi.org/10.1016/j.rsase.2021.100499>, 2021.
- Geyman, E. C. and Maloof, A. C.: A Simple Method for Extracting Water Depth From Multispectral Satellite Imagery in
635 Regions of Variable Bottom Type, *Earth Sp. Sci.*, 6, 527–537, <https://doi.org/10.1029/2018EA000539>, 2019.
- Gorelick, N., Hancher, M., Dixon, M., Ilyushchenko, S., Thau, D., and Moore, R.: Google Earth Engine: Planetary-scale geospatial analysis for everyone, *Remote Sens. Environ.*, 202, 18–27, <https://doi.org/10.1016/j.rse.2017.06.031>, 2017.
- Ha, N. T., Manley-Harris, M., Pham, T. D., and Hawes, I.: A comparative assessment of ensemble-based machine learning and maximum likelihood methods for mapping seagrass using Sentinel-2 imagery in Tauranga Harbor, New Zealand, *Remote Sens.*,
640 12, <https://doi.org/10.3390/rs12030355>, 2020.
- Hedley, J. D., Harborne, A. R., and Mumby, P. J.: Simple and robust removal of sun glint for mapping shallow-water benthos, *Int. J. Remote Sens.*, 26, 2107–2112, <https://doi.org/10.1080/01431160500034086>, 2005.
- Huisman, C. E., Bryan, K. R., Coco, G., and Ruessink, B. G.: The use of video imagery to analyse groundwater and shoreline dynamics on a dissipative beach, *Cont. Shelf Res.*, 31, 1728–1738, <https://doi.org/10.1016/J.CSR.2011.07.013>, 2011.
- 645 Hume, T., Gerbeaux, P., Hart, D., Kettles, H., and Neale, D.: A classification of New Zealand’s coastal hydrosystems, 120, 2016.

IHO, I. H. O.: ORGANISATION HYDROGRAPHIQUE INTERNATIONALE ORGANIZACION HIDROGRAFICA INTERNACIONAL IHO / OHI Publication C-55, 2020.

Jawak, S. D., Vadlamani, S. S., and Luis, A. J.: A Synoptic Review on Deriving Bathymetry Information Using Remote Sensing Technologies: Models, Methods and Comparisons, *Adv. Remote Sens.*, 04, 147–162, <https://doi.org/10.4236/ars.2015.42013>, 2015.

Jia, M., Wang, Z., Mao, D., Ren, C., Wang, C., and Wang, Y.: Rapid, robust, and automated mapping of tidal flats in China using time series Sentinel-2 images and Google Earth Engine, *Remote Sens. Environ.*, 255, 112285, <https://doi.org/10.1016/j.rse.2021.112285>, 2021.

655 Kang, Y., Ding, X., Xu, F., Zhang, C., and Ge, X.: Topographic mapping on large-scale tidal flats with an iterative approach on the waterline method, *Estuar. Coast. Shelf Sci.*, 190, 11–22, <https://doi.org/10.1016/j.ecss.2017.03.024>, 2017.

Kang, Y., Lv, W., He, J., and Ding, X.: Remote sensing of time-varying tidal flat topography, Jiangsu Coast, China, based on the waterline method and an artificial neural network model, *Appl. Sci.*, 10, <https://doi.org/10.3390/app10103645>, 2020.

Kerr, J. M. and Purkis, S.: An algorithm for optically-deriving water depth from multispectral imagery in coral reef landscapes in the absence of ground-truth data, *Remote Sens. Environ.*, 210, 307–324, <https://doi.org/10.1016/j.rse.2018.03.024>, 2018.

660 Khan, M. J. U., Ansary, M. N., Durand, F., Testut, L., Ishaque, M., Calmant, S., Krien, Y., Saifu, A. K. M., and Papa, F.: High-resolution intertidal topography from sentinel-2 multi-spectral imagery: Synergy between remote sensing and numerical modeling, *Remote Sens.*, 11, 1–20, <https://doi.org/10.3390/rs11242888>, 2019.

Khojasteh, D., Hottinger, S., Felder, S., DeCesare, G., Heimhuber, V., Hanslow, D. J., and Glamore, W.: Estuarine tidal response to sea level rise: The significance of entrance restriction, *Estuar. Coast. Shelf Sci.*, 244, 106941, <https://doi.org/10.1016/j.ecss.2020.106941>, 2020.

Khojasteh, D., Glamore, W., Heimhuber, V., and Felder, S.: Sea level rise impacts on estuarine dynamics: A review, *Sci. Total Environ.*, 780, 146470, <https://doi.org/10.1016/j.scitotenv.2021.146470>, 2021.

670 Lee, Z., Carder, K. L., Mobley, C. D., Steward, R. G., and Patch, J. S.: Hyperspectral remote sensing for shallow waters I A semianalytical model, *Appl. Opt.*, 37, 6329, <https://doi.org/10.1364/ao.37.006329>, 1998.

Li, F. K. and Goldstein, R. M.: Studies of Multibaseline Spaceborne Interferometric Synthetic Aperture Radars, *IEEE Trans. Geosci. Remote Sens.*, 28, 88–97, <https://doi.org/10.1109/36.45749>, 1990.

Liu, Y., Li, M., Zhou, M., Yang, K., and Mao, L.: Quantitative analysis of the waterline method for topographical mapping of tidal flats: A case study in the dongsha sandbank, china, *Remote Sens.*, 5, 6138–6158, <https://doi.org/10.3390/rs5116138>, 2013.

675 Lorensen, W. E. and Cline, H. E.: Marching cubes: A high resolution 3D surface construction algorithm, *Proc. 14th Annu. Conf. Comput. Graph. Interact. Tech. SIGGRAPH 1987*, 21, 163–169, <https://doi.org/10.1145/37401.37422>, 1987.

Lyzenga, D. R.: Shallow-water bathymetry using combined lidar and passive multispectral scanner data, *Int. J. Remote Sens.*, 6, 115–125, <https://doi.org/10.1080/01431168508948428>, 1985.

680 Mason, D. C. and Davenport, L. J.: Accurate and efficient determination of the shoreline in ERS-1 SAR images, *IEEE Trans. Geosci. Remote Sens.*, 34, 1243–1253, <https://doi.org/10.1109/36.536540>, 1996.

- Mason, D. C., Scott, T. R., andDance, S. L.: Remote sensing of intertidal morphological change in Morecambe Bay, U.K., between 1991 and 2007, *Estuar. Coast. Shelf Sci.*, 87, 487–496, <https://doi.org/10.1016/j.ecss.2010.01.015>, 2010.
- McFeeters, S. K.: The use of the Normalized Difference Water Index (NDWI) in the delineation of open water features, *Int. J. Remote Sens.*, 17, 1425–1432, <https://doi.org/10.1080/01431169608948714>, 1996.
- 685 Mohammadian, A., Morse, B., andRobert, J. L.: Calibration of a 3D hydrodynamic model for a hypertidal estuary with complex irregular bathymetry using adaptive parametrization of bottom roughness and eddy viscosity, *Estuar. Coast. Shelf Sci.*, 265, 107655, <https://doi.org/10.1016/j.ecss.2021.107655>, 2022.
- Morris, A. B. D., Coco, G., Bryan, K. R., Turner, I. L., Morris, B. D., Coco, G., Bryan, K. R., Turner, I. L., Street, K., andVale, M.: Video-derived mapping of estuarine evolution Stable URL : <https://www.jstor.org/stable/26481623> Linked references are available on JSTOR for this article : Video-derived mapping of estuarine evolution, 410–414, 2021.
- 690 Murray, N. J., Phinn, S. R., DeWitt, M., Ferrari, R., Johnston, R., Lyons, M. B., Clinton, N., Thau, D., andFuller, R. A.: The global distribution and trajectory of tidal flats, *Nature*, 565, 222–225, <https://doi.org/10.1038/s41586-018-0805-8>, 2019.
- Nicholls, R. J. andCazenave, A.: Sea-level rise and its impact on coastal zones, *Science (80-.)*, 328, 1517–1520, <https://doi.org/10.1126/science.1185782>, 2010.
- 695 Nobuyuki Otsu: A Threshold Selection Method from Gray-Level Histograms, *IEEE Trans. Syst. Man Cybern*, 9, 62–66, 1979.
- Oppenheimer, M., Glavovic, B., Hinkel, J., van deWal, R., Magnan, A. K., Abd-Elgawad, A., Cai, R., Cifuentes-Jara, M., DeConto, R. M., Ghosh, T., Hay, J., Isla, F., Marzeion, B., Meyssignac, B., andSebesvari, Z.: Sea Level Rise and Implications for Low Lying Islands, Coasts and Communities., *IPCC Spec. Rep. Ocean Cryosph. a Chang. Clim.*, 355, 126–129, <https://doi.org/10.1126/science.aam6284>, 2019.
- 700 Parodi, M. U., Giardino, A., VanDongeren, A., Pearson, S. G., Bricker, J. D., andReniers, A. J. H. M.: Uncertainties in coastal flood risk assessments in small island developing states, *Nat. Hazards Earth Syst. Sci.*, 20, 2397–2414, <https://doi.org/10.5194/nhess-20-2397-2020>, 2020.
- Pedrozo-Acuña, A., Ruiz de Alegria-Arzaburu, A., Mariño-Tapia, I., Enriquez, C., andGonzález Villareal, F. J.: Factors controlling flooding at the Tonalá river mouth (Mexico), *J. Flood Risk Manag.*, 5, 226–244, <https://doi.org/10.1111/j.1753-318X.2012.01142.x>, 2012.
- 705 Rueda, A., Cagigal, L., Antolínez, J. A. A., Albuquerque, J. C., Castanedo, S., Coco, G., andMéndez, F. J.: Marine climate variability based on weather patterns for a complicated island setting: The New Zealand case, *Int. J. Climatol.*, 39, 1777–1786, <https://doi.org/10.1002/joc.5912>, 2019.
- Sagar, S., Roberts, D., Bala, B., andLymburner, L.: Extracting the intertidal extent and topography of the Australian coastline from a 28 year time series of Landsat observations, *Remote Sens. Environ.*, 195, 153–169, <https://doi.org/10.1016/j.rse.2017.04.009>, 2017.
- 710 Salameh, E., Frappart, F., Marieu, V., Spodar, A., Parisot, J. P., Hanquiez, V., Turki, I., andLaignel, B.: Monitoring sea level and topography of coastal lagoons using satellite radar altimetry: The example of the Arcachon Bay in the Bay of Biscay, *Remote Sens.*, 10, 1–22, <https://doi.org/10.3390/rs10020297>, 2018.

- 715 Salameh, E., Frappart, F., Almar, R., Baptista, P., Heygster, G., Lubac, B., Raucoules, D., Almeida, L. P., Bergsma, E. W. J.,
Capo, S., DeMichele, M. D., Idier, D., Li, Z., Marieu, V., Poupardin, A., Silva, P. A., Turki, I., andLaignel, B.: Monitoring
Beach Topography and Nearshore Bathymetry Using Spaceborne Remote Sensing: A Review, *Remote Sens.*, 11,
<https://doi.org/10.3390/rs11192212>, 2019.
- Salameh, E., Frappart, F., Turki, I., andLaignel, B.: Intertidal topography mapping using the waterline method from Sentinel-
720 1 & -2 images: The examples of Arcachon and Veys Bays in France, *ISPRS J. Photogramm. Remote Sens.*, 163, 98–120,
<https://doi.org/10.1016/j.isprsjprs.2020.03.003>, 2020.
- Sobel, A. H., Camargo, S. J., Hall, T. M., Lee, C., Tippet, M. K., andWing, A. a: Cyclone Intensity, *Science (80-.)*, 353,
2016.
- Spicer, P., Huguenard, K., Ross, L., andRickard, L. N.: High-Frequency Tide-Surge-River Interaction in Estuaries: Causes and
725 Implications for Coastal Flooding, *J. Geophys. Res. Ocean.*, 124, 9517–9530, <https://doi.org/10.1029/2019JC015466>, 2019.
- Stephens, S. A., Bell, R. G., andHaigh, I. D.: Spatial and temporal analysis of extreme storm-tide and skew-surge events around
the coastline of New Zealand, *Nat. Hazards Earth Syst. Sci.*, 20, 783–796, <https://doi.org/10.5194/nhess-20-783-2020>, 2020.
- Stewart, B.: Investigating groundwater derived nutrient fluxes within Tauranga harbour, New Zealand, 1994, 2021.
- Stumpf, R. P., Holderied, K., andSinclair, M.: Determination of water depth with high-resolution satellite imagery over
730 variable bottom types, *Limnol. Oceanogr.*, 48, 547–556, https://doi.org/10.4319/lo.2003.48.1_part_2.0547, 2003.
- Tay, H. W., Bryan, K. R., DeLange, W. P., andPilditch, C. A.: The hydrodynamics of the southern basin of Tauranga Harbour,
New Zeal. *J. Mar. Freshw. Res.*, 47, 249–274, <https://doi.org/10.1080/00288330.2013.778300>, 2013.
- Traganos, D., Poursanidis, D., Aggarwal, B., Chrysoulakis, N., andReinartz, P.: Estimating satellite-derived bathymetry (SDB)
with the Google Earth Engine and sentinel-2, *Remote Sens.*, 10, <https://doi.org/10.3390/rs10060859>, 2018.
- 735 Turner, I. L., Harley, M. D., Almar, R., andBergsma, E. W. J.: Satellite optical imagery in Coastal Engineering, *Coast. Eng.*,
167, 103919, <https://doi.org/10.1016/j.coastaleng.2021.103919>, 2021.
- Vanhellemont, Q. andRuddick, K.: Atmospheric correction of metre-scale optical satellite data for inland and coastal water
applications, *Remote Sens. Environ.*, 216, 586–597, <https://doi.org/10.1016/j.rse.2018.07.015>, 2018.
- Vos, K., Splinter, K. D., Harley, M. D., Simmons, J. A., andTurner, I. L.: CoastSat: A Google Earth Engine-enabled Python
740 toolkit to extract shorelines from publicly available satellite imagery, *Environ. Model. Softw.*, 122, 104528,
<https://doi.org/10.1016/j.envsoft.2019.104528>, 2019.
- Van DerWalt, S., Schönberger, J. L., Nunez-Iglesias, J., Boulogne, F., Warner, J. D., Yager, N., Gouillart, E., andYu, T.:
Scikit-image: Image processing in python, *PeerJ*, 2014, 1–18, <https://doi.org/10.7717/peerj.453>, 2014.
- Wankang, Y., Baoshu, Y., Xingru, F., Dezhou, Y., Guandong, G., andHaiying, C.: The effect of nonlinear factors on tide-
745 surge interaction: A case study of Typhoon Rammasun in Tieshan Bay, China, *Estuar. Coast. Shelf Sci.*, 219, 420–428,
<https://doi.org/10.1016/j.ecss.2019.01.024>, 2019.

Webster, P. J., Holland, G. J., Curry, J. A., and Chang, H. R.: Atmospheric science: Changes in tropical cyclone number, duration, and intensity in a warming environment, *Science* (80-.), 309, 1844–1846, <https://doi.org/10.1126/science.1116448>, 2005.

750